The Astronomical Journal, 133:862–881, 2007 March

THE ACTIVITY AND VARIABILITY OF THE SUN AND SUN-LIKE STARS. I. SYNOPTIC Ca II H AND K OBSERVATIONS

Jeffrey C. Hall, G. W. Lockwood, and Brian A. Skiff
Lowell Observatory, Flagstaff, AZ, USA
Received 2006 August 24; accepted 2006 October 20

ABSTRACT

Synoptic measurements of activity in Sun-like stars have been performed continuously since 1966, and the largest set comes from the Mount Wilson HK project, in the form of the well-known *S* index. We have been monitoring the activity and variability of the Sun and a large sample of Sun-like stars, in terms of *S* and absolute flux, since 1994 with the Solar-Stellar Spectrograph (SSS) at Lowell Observatory. Directly inspired by the similar long-term program at Mount Wilson Observatory, the SSS incorporates both an HK spectrograph and an echelle for visible and far-red observations. This is the first of three papers presenting the results of some 20,000 observations of the Sun and Sun-like stars with the SSS. In this paper we describe our program, review the calibration of solar and stellar fluxes to *S* and the chromospheric emission fraction R'_{HK}, compare our derived stellar activity measures to those from other programs, and discuss the broad characteristics of the activity and variability in our target set, with particular attention to good solar analogs and noncycling stars. In subsequent papers we will discuss the echelle data and present detailed examinations of stars of particular interest.

Key words: stars: activity — Sun: activity

1. INTRODUCTION

1.1. *Overview of Stellar Cycles Research*

In a paper described as a "minor contribution," Eberhard & Schwarzschild (1913) wrote, "Reversals of lines in stellar spectra are not rare…It remains to be shown whether the emission lines of the star have a possible variation in intensity analogous to the sun-spot period."

This minor contribution has generated a certain amount of attention to the matter, including 40 years of Ca II H and K observations at Mount Wilson Observatory (MWO) pursuant to the question posed by Wilson (1978), "Does the chromospheric emission of main sequence stars vary with time, and if so, how?" That seminal paper answered the question in the affirmative and demonstrated the existence of various types of cyclic and noncyclic variability in (not necessarily Sun-like) stars. Following Wilson's retirement, the MWO program continued under the direction of S. Baliunas, resulting in publication of much of the database (Duncan et al. 1991) and a major summary of some 30 years of observations of the familiar MWO *S* index of stellar chromospheric activity (Baliunas et al. 1995, hereafter B95), among numerous other papers. Further work (Baliunas et al. 1998) indicated that 60% of lower main-sequence stars exhibit periodic variations akin to the solar cycle, 25% are variable with no well-defined periodicity, and 15% are constant with time—the so-called flat activity (FA) stars.

A program of synoptic photometry of Sun-like stars has proven to be an invaluable complement to the spectroscopic MWO observations. From 1984 to 1998, R. Radick and his collaborators observed 35 MWO stars in Strömgren *b* and *y*, finding that the total stellar irradiance varied inversely with chromospheric activity for young stars and, as is the case for the Sun, directly with activity for old stars (Lockwood et al. 1992a, 1997; Radick et al. 1998). Precision photometry of Sun-like stars continues today at the Fairborn Observatory in southern Arizona (Henry 1999).

An interesting result of the synoptic photometric and spectroscopic surveys is the photometric quiescence of the Sun relative to its closest stellar cousins. The well-established 0.1% variation in total solar irradiance (TSI) from cycle minimum to maximum (e.g., Fröhlich 2000) is markedly smaller than most stars of similar T_{eff}, yet the Sun has a vigorous chromospheric cycle, as manifested in the Ca II H and K proxy (Radick et al. 1998). The search for these "solar analogs" was started by Hardorp (1978) and was reviewed in detail by Cayrel de Strobel (1996). Recently, a list of the "Top Ten solar analogs" appeared (Soubiran & Triaud 2004); one of these is the well-known "solar twin" 18 Sco, first identified as such by Porto de Mello & da Silva (1997). Intensive observations of these and similar stars continue today at Lowell and Fairborn.

Since 1974, workers at the National Solar Observatory (NSO) have made observations of the Sun in Ca II H and K (e.g., White & Livingston 1978, 1981; White et al. 1998). These observations, now spanning more than a Hale cycle, underpin our present understanding of the relationship between solar activity and TSI. The NSO data have also been used in conjunction with the MWO data to infer the magnetic state of the noncycling Sun (White et al. 1992), a critical question in light of the well-known Maunder minimum of 1645–1715 (Eddy 1976), in which the solar cycle dropped to a greatly reduced amplitude (Ribes & Nesme-Ribes 1993) and—perhaps not by coincidence—episodes of severe winter weather associated with the Little Ice Age of ~1300–1715 ravaged Europe.

Since the early facular-excess/sunspot-deficit models (Lean & Foukal 1988; Foukal & Lean 1990), the various TSI reconstructions have been essential in assessing the role of the Sun in driving terrestrial climate change. Irradiance variations much greater than the currently observed 0.1% have been proposed (e.g., Lean et al. 1995; Fligge & Solanki 2000), but recent models suggest these larger variations may be exaggerated (Wang et al. 2005). The magnetic activity of cycling and noncycling Sun-like stars (e.g., Baliunas & Jastrow 1990; Zhang et al. 1994) has guided many reconstructions of the Maunder minimum Sun, and an assessment of these stellar characteristics is an essential part of our present program.

The foregoing is merely a starting point for working back into a huge body of literature and is meant to put our own observations into context. Detailed reviews are presented by (among others) Baliunas & Vaughan (1985), Radick (1992), Haisch & Schmitt (1996), and Strassmeier (2005).

1.2. *Characterizing Stellar Activity*

In the papers in this series, we are concerned with stellar activity as manifested not only in the Ca II H and K lines but also in a number of activity proxies in the visible and far-red. Evaluation of data sets discussing activity in the visible is simplified by the lower line blanketing in these spectral regions, and the calibrations will be treated in the second paper in this series. More difficult are the HK observations, which are the subject of the present paper.

The original and most extensive set of HK observations comes from the two spectrophotometers used in the MWO survey, dubbed the HKP-1 (used from 1966 through 1977) and HKP-2 (put into service in 1977 April). Solar and stellar activity from the MWO program are expressed in terms of the familiar S index, which is first described by Vaughan et al. (1978). It is a dimensionless, color-dependent quantity that is essentially the ratio of flux in the HK line cores to that in two nearby continuum bandpasses. Vaughan et al. (1978) also established the transformation by which the 12 yr of HKP-1 measurements, which used a similar activity index, could be transformed to S.

A number of other synoptic solar and stellar activity programs have emerged since Wilson began his work, including the Solar-Stellar Spectrograph (SSS) project. Installation of the HKP-2 also roughly coincided with the advent of large volumes of flux-calibrated cool star data from satellite observatories such as *Einstein* and *IUE*. Shortly after the definition of S, therefore, it became advantageous to establish (1) transformations between other instrumental data and S and (2) a method for converting S to flux. At the same time, debate regarding the photospheric contribution to emission in the HK line cores (Blanco et al. 1974, 1976; Linsky & Ayres 1978) and the desire to remove it to isolate ostensibly dynamo-driven variations led to the formulation of the familiar chromospheric emission fraction parameter $R'_{\rm HK}$ (Hartmann et al. 1984; Noyes et al. 1984), in which S is converted to the bolometric flux fraction $R_{\rm HK}$ and then corrected by removing an empirically determined photospheric contribution $R_{\rm phot}$. However, interpretation of $R'_{\rm HK}$ is further complicated by the mixing of wing (i.e., photospheric) magnetic, radiative equilibrium (RE), and so-called basal components in the emission (e.g., Schrijver et al. 1989b) for any of the instrumental bandpasses under consideration.

Our approach to characterizing stellar activity in this paper is to first examine methods for determining the absolute flux in our solar and stellar HK data and to ensure that these measurements are consistent with ensemble measurements of S and $\log R'$. However, in this work we use S and $\log R'$ primarily as hooks that (1) allow comparison with other data sets, creating confidence in the accuracy of our reductions and flux measurements, and (2) allow us to comment on patterns in our data relative to those in other synoptic studies (e.g., B95; Radick et al. 1998; Gray et al. 2003; Wright et al. 2004). For the bulk of our discussion, we rely on the absolute flux as the fundamental datum and examine the various components of the fluxes to isolate and examine the magnetic behavior of the closest solar analogs over a period of 10 yr.

1.3. *Organization of This Paper*

We begin by discussing our observing program and data reduction methods (in § 2), and we evaluate the methods and results of determining absolute HK fluxes for the Sun and Sun-like stars (§ 3). In § 4 we review the measurement and interpretation of emission in the HK lines. Efforts to reconcile the various quantities discussed in § 1.2 have had varying degrees of success. We therefore spend some time discussing (1) methods for determining the absolute fluxes at the surfaces of Sun-like stars, (2) the ways by which workers have transformed S to flux, (3) the agreement (or lack thereof) between the derived quantities and S for different programs and different stellar targets, and (4) the conversion of S to physically interpretable quantities. With the details of measurement and calibration in place, we present and discuss our HK results in § 5.

2. PROGRAM DESCRIPTION

2.1. *Instrumentation*

The SSS was built in the late 1980s at the High Altitude Observatory (HAO) in Boulder, Colorado. Initial data were obtained after installation at Lowell's 1.1 m John Hall telescope in 1989. After a funding hiatus, the project was restarted in 1992. Following replacement of some hardware and computer components, as well as installation of an autoguider and exposure meter, regular observations began in late 1993, and we have maintained a steady observing cadence since then.

The spectrograph is permanently associated with the 1.1 m telescope, which is at Lowell's Anderson Mesa dark-sky site about 6 miles (9.5 km) southeast of Flagstaff. The spectrograph is fed by an optical fiber system that allows both sunlight and starlight to be directed into the spectrograph from a single input fiber. The solar "telescope" is an optical fiber that observes the Sun as an unresolved, full-disk source; it is mounted on the south side of the dome. This fiber goes to a junction box at the telescope, in which sunlight is reflected to the stellar input fiber mounted at the telescope focus. Flat-field and calibration lamp light can also be directed into the stellar fiber via the same junction box, and this single fiber then goes to the spectrograph input. Therefore, all of the SSS's light sources emerge into the spectrograph as a uniform f/8 beam from one fiber, ensuring that sunlight and starlight enter and are propagated identically through the spectrograph optics.

The first optical element is a dichroic beam splitter, and the SSS actually comprises two completely distinct spectrographs. Near-UV light is directed to a single-order "blue" spectrograph, and visible and far-red light passes to an echelle "red" spectrograph. The detectors are TEK 512×512 CCDs; they are old and noisy (42 electron read noise), but our targets are extremely bright ($V \leq 7.5$) and the detectors are adequate for the task. The analog-to-digital converter is 14 bit, and the detector response is linear to 15,000 ADUs. The Ca II H and K order recorded by the blue spectrograph covers $\lambda 3860$ to $\lambda 4011$ at a resolution of approximately 0.29 Å. The hardware system is a testament to the talents of the HAO engineers; except for periodic minor problems, it has performed flawlessly for some 20,000 observations representing (when individual exposures in averaged frames of the Sun and flat fields are taken into account) roughly 300,000 CCD readouts.

However, the age of the CCDs, the relatively low total system throughput, the modest telescope aperture, and the need for a reasonable observing cadence for many stars limits us to bright targets. Our canonical exposure guideline is 10 minutes for a star of $V = 5.0$. Although we can obtain passable spectra of targets with $V = 10$, we have dropped all but a very few stars fainter than 7.0 from our observing list, as we cannot obtain a good signal-to-noise ratio (S/N) and sufficiently well-sampled H and K series for these targets without severely curtailing our target list. This is a significant limitation, given the present interest in observing good solar analogs and their relative paucity in the Bright Star Catalogue.

2.2. *Observing Program*

Although the SSS is computer-operated, an observer is required to take and verify the data quality of every exposure. For the stellar observing program, we are typically assigned about 10 nights of bright time per month. Historically, about 30% of these nights have been photometric, 30% spectroscopic, and 40% partly or completely cloudy; we therefore typically obtain five to six usable nights per month, averaging from 20 to 40 targets per night depending on the time of year.

To ensure optimal coverage of the most important targets, we have divided our observing list into three priority levels, with the best solar analog stars assigned to the priority 1 list (observed every night during their observing season), and progressively less Sun-like stars assigned to priority 2 (observed at least twice per monthly run) or priority 3 (at least once per run). Priority level memberships and observing frequency have been determined partly through experience; the present target list and priority distribution yields a yearly observing burden close to what local weather statistics indicate we can obtain. At present, we have 18 priority 1 stars, 32 priority 2 stars, and 93 priority 3 stars.

The arrangement of the SSS fiber feeds allows us to carry out solar observations regardless of whether the stellar instrumentation is attached to the telescope. We therefore average about two to three solar observations per week, with a time burden (including commute to the dark-sky site) of 2–3 hr per observation. A "solar observation" consists of 48 individual exposures of the Sun, reduced to three 16 frame averages, plus a 16 frame averaged flat field.

Every frame acquired on the stellar and solar programs is assigned a running frame number, and the raw data are stored in FITS format. Including flat field, bias, dark, and Th-Ar calibration frames, as of 2006 June 30 we had accumulated 18,774 stellar frames and 5503 solar frames, with observations taken by the authors and a number of student observers over the years. We acquire flats with every day's observations, but we take biases, darks, and Th-Ar emission spectra only occasionally as checks on the instrumental stability (spectra are debiased using individual frame backgrounds and are set to zero velocity in reduction for analysis of variations in the spectral lines). Bad frames are deleted during reduction preprocessing, observation records are stored in electronic logs, and reduction of the raw data to reduced spectra proceeds as described in § 2.3.

2.3. *Reducing the HK Data*

The SSS Ca II H and K and echelle data are recorded on two different CCDs, each with its own peculiarities. The raw data image is a 512×400 pixel grafted composite of the relevant parts of the echelle ("red") and HK ("blue") CCDs.

In this paper we discuss the reduction of the "blue" spectrum, which is the single-order spectrum covering $\lambda3860$ to $\lambda4010$. Reduction of the echelle data is not pertinent to the results of this paper and is deferred to the next paper in this series.

All SSS raw frames are reduced to continuum-normalized spectra using IDL routines written in-house. As the data set has grown over the years, our original procedural library has been replaced by an object-oriented library that can, if we choose, reduce a decade of data with one command. We can also reduce data and produce the essential output products by a range of dates or for a desired star or set of stars. Each of our solar and stellar HK observations is reduced via the following steps:

Preprocessing.—Every solar and stellar data frame has an associated entry in our electronic log files. Before reduction, we preprocess the frame by rotating it so the dispersion axis of the orders is optimized for fast IDL processing, and we create and prepend a FITS header using data extracted from the log files.

Bias and scattered light removal.—The blue frame in an SSS spectrum is a 512×32 pixel rectangle with the order centered on the long axis. We determine and remove the electronic bias and scattered light by performing two traces along the order, well outside the 9 pixel wide order aperture. We are able to adopt this relatively simple technique for removing the scattered light because the blue spectrograph is not an echelle but a single-order instrument employing a single grating, and difficulties with scattered light or faint ghost orders introduced by the cross-disperser are not present. We monitor any potential scattered light introduced by the grating through comparison of the inner H and K line profiles with high-resolution solar spectra degraded to the resolution of the SSS. Significant scattered light in the H and K line cores would manifest itself as a systematic overestimation of activity diagnostics for inactive and/or cooler stars. We quantify this using solar spectra taken near activity minimum (~1996 and ~2006); where minimum high-resolution NSO full-disk HK indices are ~86 mÅ (White & Livingston 1978), our mean indices near solar minimum are ~89 mÅ. This higher number results from a combination of our lower resolution and any scattered light that slightly fills in the line cores, and it sets an upper limit in our HK spectra of ~4% for the contribution by scattered light for the Sun and similarly inactive solar analogs. As shown in § 3, the calibration of our derived stellar H and K surface fluxes appears to be of uniform quality for all spectral types and activity levels found in our target set.

Order tracing.—We create order maps using flat-field quartz lamp spectra. The almost perfectly straight HK order is centered on row 16 of the 32 row image. We fit Gaussians to six evenly spaced profiles along the HK order of the flat-field spectrum, and a second-order polynomial is fit to the six centroids. The centroids at every pixel, as determined from the fit coefficients, are stored as the 512×20 order map for that flat field, and this map of centroids specifies the order locations for all solar or stellar frames for the remainder of the reduction process. (The second-order polynomial is used to accommodate the curvature of the echelle orders, which are reduced at the same time as the HK order; for the single-grating blue spectrograph, the second-order coefficient of the order trace is effectively zero.)

Flat fielding.—To remove pixel-to-pixel gain variations, we extract the spectrum of the flat-field frame, normalize the flat-field continuum in each order to unity, and then divide each pixel within the order apertures of the target frames by the corresponding normalized flat-field value. This preserves the original counts in the target frames. Since we divide all 9 pixels across an extraction aperture at order x, pixel y by the single flat-field value corresponding to that pixel, this method assumes that pixel-to-pixel gain variations across the aperture are small, and the almost precisely Gaussian shape of the aperture profiles suggests this is the case.

Spectrum extraction and application of wavelength calibration.—Using the order map as a reference, we can now extract and normalize the target spectra. For our relatively high S/N spectra, we use a profile-weighted extraction procedure to produce the raw spectra, wherein the sky-subtracted profile is weighted by a normalized profile model, giving the highest weight to pixels nearest the center of the aperture (and hence having the highest S/N). The procedure follows that described by Wagner (1992).

We have calculated the wavelength solution using a Th-Ar hollow cathode. Since our resolution is insufficient for high-precision velocity work, and since velocities are not central to our program, we spend observing time on Th-Ar frames only intermittently as a

TABLE 1
Priority 1 Stars

HD (1)	Name (2)	Spectral Type (3)	V (4)	$B-V$ (5)	$b-y$ (6)	Other Programs (7)
4307	18 Cet	G0 V	6.15	0.60	0.394	APT
10307	HR 483	G1 V	4.96	0.62	0.390	APT, ELODIE
10700	τ Cet	G8 V	3.50	0.72	0.438	MWO, APT
30495	58 Eri	G1.5 V	5.51	0.64	0.403	MWO, APT
38858	HR 2007	G2 V	5.97	0.64	0.401	APT
41330	HR 2141	G0 V	6.10	0.60	0.389	...
52711	HR 2643	G0 V	5.93	0.60	0.382	...
60803	HR 2918	G0 V	5.91	0.60	0.380	...
76151	HR 3538	G2 V	6.00	0.67	0.416	MWO, APT
95128	47 UMa	G1 V	5.05	0.61	0.392	APT, ELODIE
140538	ψ Ser	G5 V	5.84	0.68	0.421	APT
146233	18 Sco	G2 Va	5.49	0.65	0.409	APT, ELODIE
157214	72 Her	G0 V	5.39	0.62	0.402	APT
186408	16 Cyg A	G1.5 Vb	5.95	0.64	0.409	APT
186427	16 Cyg B	G3 V	6.20	0.66	0.416	MWO, APT, ELODIE
187923	HR 7569	G2 V	6.16	0.65	0.411	APT
190406	15 Sge	G0 V	5.80	0.61	0.384	MWO, APT
225239	HD 9107	G2 V	6.12	0.62	0.412	...

consistency check. Spectra are placed on the reference wavelength grid with velocities zeroed prior to time series generation.

Normalization.—We place the HK spectra on an absolute intensity scale, with the continuum set to 1.0 across our entire spectral coverage, by fitting the extracted spectrum with a piecewise linear fit through several points between $\lambda3860$ and $\lambda4000$ for which we have empirically determined absolute intensity values using available solar and stellar spectrophotometry and line-blanketing coefficients. The spectra thus normalized are both internally and externally self-consistent (i.e., our raw solar and stellar HK indices and derived S values agree well with those derived from other studies), and our normalized spectra are well matched by the high-resolution Kurucz et al. (1984, hereafter K84) solar spectrum degraded to the resolution of the SSS.

2.4. *Targets*

The SSS target list includes 143 Sun-like stars, in addition to the Sun. All but four of the targets have $V \leq 7.5$ and are primarily drawn from the Supplement to the Bright Star Catalogue. As noted above, the stars are divided into three priority levels, with priority 1 stars being observed every clear night during our runs and their observing seasons. The priority categorizations roughly parallel the solar twin/solar analog/Sun-like star criteria of Cayrel de Strobel (1996), and the full target list encompasses all but about 14 of the stars on the main MWO list (B95), the ELODIE Top Ten solar analogs (Soubiran & Triaud 2004), and about 100 stars on the Tennessee State University Automated Photometric Telescope (APT) program (G. W. Henry 2004, private communication).

Our present priority scheme was set up in 1996, and a few stars have been shuffled as the program has evolved. A final review of the priority scheme was made in mid-2004, following suspension of observations at MWO and the subsequent addition of about 35 MWO stars not previously on our program (to preserve their observational time series) to the SSS target list.

In Tables 1 and 2 we list the 50 stars on our priority 1 and 2 target lists. They are broken into separate tables to facilitate comparison of the photometric properties. Stars on these two priority levels encompass the majority of observations taken with the SSS thus far. The complete target list, including all priority 3 stars, is available on the SSS Web site.[1]

3. MEASURING SOLAR AND STELLAR RADIATION

3.1. *The Solar Irradiance and Surface Flux*

An essential aspect of our program is assessment of the Sun's behavior relative to its nearest stellar cousins, for which an absolutely calibrated solar spectrum is a necessary starting point. The solar irradiance spectrum has been measured from the ground (Lockwood et al. 1992b; Neckel & Labs 1984), from airplanes (e.g., Arvesen et al. 1969; Thekaekara et al. 1969), and from space (e.g., Thuillier et al. 1998) over varying wavelength regimes and with results presented in the literature with the usual panoply of units. For this work we adopt the composite spectra of Thuillier et al. (2004, hereafter T04), who have reviewed the available data and constructed two reference solar irradiance spectra for high and low levels of solar activity (the epochs of the ATLAS 1 and ATLAS 3 space shuttle experiments of 1992 March and 1994 November, respectively), from the far-UV to the infrared.

The composite spectrum of T04 employs the mean of the ATLAS SOLSPEC spectra for nearly the entire region covered by the SSS echelle (5000–9000 Å) and the mean of five data sets (two UARS instruments and three ATLAS instruments) in the near-UV. For this spectral region (between $\lambda2000$ and $\lambda4000$), T04 find the agreement between the mean ATLAS and UARS spectra to be 0.5% and the rms differences of the data sets to be 2%. The effect of the solar cycle variations on irradiance in this part of the spectrum is negligible (Fontenla et al. 1999). The resolution of these spectra is 2.5 Å at Ca II H and K and 5 Å in the visible and near-IR, with a sampling interval of 0.05 Å. Thuillier et al. (1998) report the total error on the underlying SOLSPEC data to be 4.3% at $\lambda3700$. Since instrumental effects such as scattered light can significantly affect the calibration in the H and K line cores, we use this reference spectrum only to obtain estimates of the surface flux in the continuum in bandpasses corresponding to those of the MWO HKP-2 ($\lambda3891$ to $\lambda3911$ and $\lambda3991$ to $\lambda4011$), interpolating

[1] The target list, along with reduction details, program status and updates, and other resources, may be found at http://www.lowell.edu/users/jch/sss/index.php.

TABLE 2
PRIORITY 2 STARS

HD	Name	Spectral Type	V	$B-V$	$b-y$	Other Programs
1461	HR 72	G3 V	6.46	0.68	0.422	APT
1835	9 Cet	G5 V	6.39	0.66	0.412	MWO, APT
9562	HR 448	G1 V	5.75	0.64	0.408	MWO, APT
10476	107 Psc	K1 V	5.24	0.84	0.492	MWO
10780	HR 511	G9 V	5.63	0.81	0.468	MWO
20630	κ Cet	G5 V	4.84	0.68	0.420	MWO, APT
22049	ε Eri	K2 V	3.73	0.88	0.498	MWO, APT
35296	111 Tau	F8 V	5.01	0.53	0.345	MWO, APT
39587	χ^1 Ori	G0 V	4.41	0.59	0.376	MWO, APT
42807	HR 2208	G5 V	6.44	0.66	0.418	APT
43587	HR 2251	G0 V	5.71	0.61	0.385	MWO, APT
71148	HR 3309	G1 V	6.36	0.63	0.402	ELODIE
75528	54 Cnc	G5 V	6.38	0.64	0.415	...
81809	HR 3750	G0+G9	5.38	0.64	0.415	MWO, APT
81858	ω Leo	F9 V	5.41	0.60	0.391	...
82885	11 LMi	G8+V	5.41	0.77	0.473	MWO, APT
88986	24 LMi	G2 V	6.46	0.60	0.397	APT
89269	SAO 43729	G6 V	6.65	0.65	0.420	APT, ELODIE
90508	HR 4098	G0 V	6.45	0.60	0.397	APT
97334	HR 4345	G1 V	6.41	0.61	0.391	MWO, APT
114710	β Com	G0 V	4.26	0.58	0.367	MWO
126053	HR 5384	G1.5 V	6.27	0.63	0.405	MWO, APT
141004	λ Ser	G0 IV–V	4.43	0.60	0.382	MWO, APT
142373	χ Her	G0 V	4.62	0.57	0.382	MWO
143761	ρ CrB	G0 V	5.40	0.60	0.393	MWO, APT
168009	HR 6847	G1 V	6.30	0.65	0.411	APT, ELODIE
181655	HR 7345	G5 V	6.29	0.67	0.420	APT
185144	σ Dra	G9 V	4.69	0.80	0.475	MWO, APT
197076	HR 7914	G1 V	6.44	0.60	...	APT
198802	HR 7994	G5 V	6.38	0.66	0.414	APT
217014	51 Peg	G2 V+	5.50	0.68	0.417	MWO, APT
224930	85 Peg	G5 V	5.75	0.67	0.428	...

the surface flux in the continuum at $\lambda3950$ from these values. We then use this value to convert our HK spectra, normalized to unity by our reduction routines, to absolute flux.

Figure 1 shows the region of the T04 spectrum of interest. Gray areas show the spectral coverage of the SSS. At left is the single order of the blue spectrograph, covering the Ca II H and K lines. At right are the 19 orders of the echelle, with incomplete coverage from roughly the Mg I b lines at $\sim\lambda5170$ to the far-red, including the $\lambda8498$ and $\lambda8542$ lines of the Ca II infrared triplet.

The inset in Figure 1 shows the T04 irradiance spectrum for the wavelengths covered by the SSS Ca II H and K order, with the T04 irradiances converted to flux at the surface of the Sun via the simple factor $(1\ \mathrm{AU}/R_\odot)^2$. Taking the AU to be 1.496×10^{13} cm and the solar diameter to be 6.96×10^{10} cm, this factor is 46,200. The line blanketing at 1 Å intervals was then calculated by degrading the K84 high-resolution spectrum to the resolution of T04 and dividing the flux-converted T04 data by the blanketing at each bandpass. The continuum thus obtained is shown at 1 Å intervals for each of the reference windows of the HKP-2 spectrometer (Fig. 1, *diamonds*). The dotted line shows the continuum obtained over the whole spectrum, illustrating the sensitivity to uncertainties in H and K line core regions. A linear fit to the two continuum reference regions yields a smooth estimate for the continuum flux across the entire SSS H and K spectrum, as well as for the bandpasses of the HKP-2.

3.2. *Motivation for Empirical Flux Scales*

For the most direct physical comparison of solar analogs with the Sun, it is desirable to express solar and stellar activity in physical units. The difficulty of absolute stellar surface flux measurement, however, has led to widespread use of relative indices such as MWO S and the NSO HK index (e.g., White & Livingston 1978). While such measures are internally self-consistent, the flux associated with them varies with effective temperature, complicating the physical interpretation of the behavior of a stellar ensemble. Therefore, from the outset of the SSS program, we have employed methods to convert HK indices and S to surface flux. A number of other workers have done this as well. However, while measuring the HK index is quite straightforward, conversion to surface flux introduces all the usual problems with absolute measurements, and discrepancies of as much as 25%, particularly in the more heavily blanketed parts of the spectrum, remain in the literature.

To express our Ca II H and K and echelle results in absolute flux units, we require surface flux estimates for a variety of Sun-like stars in the approximate range $0.4 \le B-V \le 1.2$. Vega (Hayes & Latham 1975), 109 Vir (Tüg et al. 1977), and a handful of somewhat fainter stars (e.g., Breger 1976) are the absolutely calibrated standards to which other published stellar energy distributions are calibrated. Derivation of the surface fluxes, however, requires knowledge of the stellar angular diameters, which are typically <1 mas for cool dwarfs at 10–25 pc and are therefore available for few of our targets. This difficulty has led a number of authors to derive relations expressing absolute stellar surface fluxes, in various bandpasses of interest, as functions of broadband color indices, mostly Johnson colors. While such empirical flux scales are typically accurate to only 10%–25%, they permit estimation of stellar surface fluxes for many more targets than is

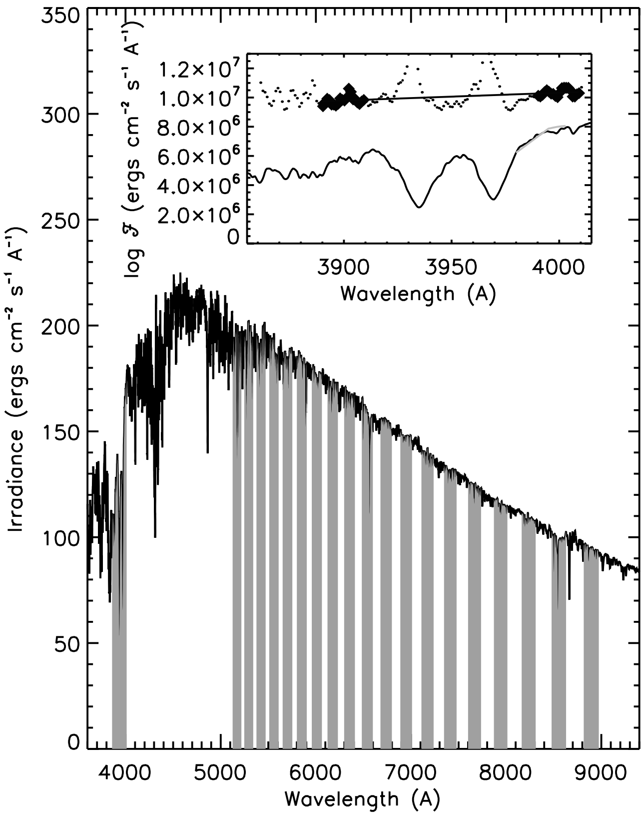

Fig. 1.—T04 solar irradiance spectrum over the wavelength range of interest for this paper. Gray bars show the spectral coverage of the SSS (*left*, HK order; *right*, 19 echelle orders). The inset shows the continuum calibration in the HK region. The irradiance spectrum, converted to flux as described in the text, is shown for the spectral coverage of the SSS HK order. Diamonds show the continuum derived (at 1 Å intervals and 2.5 Å resolution) by deblanketing the irradiance spectrum with the degraded K84 solar spectrum. These areas match the blue and red reference bandpasses of the MWO HKP-2 and provide reasonably consistent continuum estimates. The dotted line shows the less reliable continuum obtained in areas with stronger lines. A linear fit to the reference bandpasses is used to arrive at estimates of the solar continuum flux at the H and K line centers.

possible with available spectrophotometry and diameter measurements. Below, we review the extant stellar flux scales and evaluate them in light of available photometry, as well as the T04 solar irradiance calibration.

3.3. *Evaluation of HK Flux Scales and the Solar Flux*

Linsky et al. (1979, hereafter L79) created an initial stellar flux scale at the Ca II H and K bandpass for use in their model stellar chromospheres. They used an early and comprehensive set of stellar surface flux measurements by Willstrop (1965), who published spectrophotometry of 215 stars, spanning spectral types O5 to M4 and luminosity classes I–V. Although this paper presents data only down to λ4000, L79 obtained Willstrop's H and K region data via private communication. Using the Barnes-Evans relation (Barnes & Evans 1976; Barnes et al. 1976), which allows estimation of a star's diameter from its Johnson $V-R$, L79 converted the fluxes at Earth to absolute surface fluxes, obtaining an empirical relationship for estimating the surface flux in the bandpass λ3925 to λ3975 for dwarfs and giants alike from its broadband photometry:

$$\log \mathcal{F}(\Delta\lambda) = 8.264 - 3.076(V-R) \text{ for } V-R < 1.30. \quad (1)$$

By this relationship, the solar surface flux from λ3925 to λ3975 is 4.30×10^6 ergs cm^{-2} s^{-1}, where L79 took $(V-R)_\odot = 0.53$. The total blanketing in this bandpass as measured from K84 is 60.0%, so the derived continuum flux at the solar surface is 1.08×10^7 ergs cm^{-2} s^{-1}, only 8% higher than that determined from the T04 irradiance spectrum and well within L79's quoted 15% probable uncertainty on the flux scale.

Although $V-R$ has the advantage of relative insensitivity to metallicity, $B-V$ is much more commonly available. Beasley & Cram (1993, hereafter BC93) used the same data as L79 to construct an analogous surface flux relation in terms of $B-V$, obtaining

$$\log \mathcal{F}(\Delta\lambda) = 8.05 - 2.20(B-V) \text{ for } -0.1 \leq B-V \leq 1.35. \quad (2)$$

If we take $(B-V)_\odot = 0.64$ (Cayrel de Strobel 1996) and convert to continuum flux, we obtain 1.10×10^7 ergs cm^{-2} s^{-1}.

The main sources of error in either of these relations arise from errors in the underlying spectrophotometry (stated by Willstrop [1965] to be $\sim$10%) and in the stellar angular diameters obtained from the Barnes-Evans relation. Further complicating use of this empirical flux scale for the Sun is the ongoing uncertainty in $(B-V)_\odot$; published results include 0.628 (Taylor 1998), 0.66 (Hardorp 1980), 0.68 (Lang 1992), and 0.686 (Tüg & Schmidt-Kaler 1982). Changing $(B-V)_\odot$ from 0.63 to 0.67 results in a 22% change in the derived solar surface flux.

Pasquini et al. (1988) examined absolute Ca II H and K line profiles using a similar approach. Their small bandpass precluded use of the L79 method, but their independent determination of stellar surface fluxes at λ3950.5 yields a solar continuum flux of 1.10×10^7 ergs cm^{-2} s^{-1} Å^{-1}.

Hall (1996, hereafter H96) examined the empirical flux scale process in detail for four color indices (Johnson $B-V$, $V-R$, and $R-I$ and Strömgren $b-y$) and in three different bandpasses (H and K, the Ca II infrared triplet, and Hα). This work endeavors to directly obtain the flux in the continuum rather than the line-blanketed surface fluxes, which is especially difficult in the HK region due to the heavy blanketing. The results from the various HK flux scales are collected in Table 3. In this table, the $R-I$ and $b-y$ colors of the Sun are taken to be 0.330 and 0.409, respectively; these are estimates based on the same color indices of the solar twin HD 146233 (18 Sco) and the solar analog HD 186408 (16 Cyg A). The results of H96 are all in agreement within the estimated errors, although the H96 $B-V$ scale falls on the low side by about 12%.

The various flux scales described above are shown in Figure 2. We show six flux scales based on a variety of color indices (Johnson $B-V$ and $V-R$ and Strömgren $b-y$). The correspondence between these quantities is, of course, not 1:1, so the relative axis scaling is approximate and is meant to provide a general idea as to the agreement (or lack thereof) between the flux scales.

The two dotted lines (lines 5 and 6) are blanketed surface flux scales of BC93 (line 5) and L79 (line 6). The deblanketed (continuum) versions of these flux scales are shown as dashed lines labeled 3 (L79; discussed by Duncan et al. 1991) and 1 (BC93; deblanketed using measured blanketing in SSS spectra of a variety of stars from late A to K). Also shown are the $B-V$ and $b-y$ continuum flux scales published by H96 (lines 2 and 4, respectively).

The blanketed surface flux and continuum flux at λ3925 to λ3975 for the Sun, using the T04 irradiance, are shown as open and filled diamonds, respectively, and the gray area indicates the color range of roughly 90% of the stars in the SSS target list.

TABLE 3

Solar Ca ii H and K Surface Flux in the Continuum Obtained via Different Flux Scales

Method (1)	$\mathcal{F}(3925–3975)$[a] (2)	References (3)
Irradiance measurement	$(1.00 \pm \sim 0.05) \times 10^7$	T04
Empirical flux scale $(V-R)_J$, deblanketed per K84	$(1.08 \pm \sim 0.11) \times 10^7$	L79
Empirical flux scale $(B-V)$, deblanketed per K84	$(1.10 \pm \sim 0.12) \times 10^7$	BC93
Empirical flux scale $(V-R)_J$[b]	$(1.10 \pm \sim 0.22) \times 10^7$	P88[c]
Empirical flux scale $(B-V)$[b]	$(0.88 \pm \sim 0.10) \times 10^7$	H96
Empirical flux scale $(V-R)_J$[b]	$(0.96 \pm \sim 0.18) \times 10^7$	H96
Empirical flux scale $(R-I)_J$[b]	$(1.03 \pm \sim 0.19) \times 10^7$	H96
Empirical flux scale $(b-y)$[b]	$(1.00 \pm \sim 0.12) \times 10^7$	H96

[a] Solar continuum flux near Ca ii H and K, in ergs cm^{-2} s^{-1} Å^{-1}.
[b] Solar colors determined as described in the text.
[c] P88: Pasquini et al. (1988).

We consider Figure 2 in the regimes of solar analogs, warm stars, and cool stars. First, there is broad agreement in surface flux estimates for the region of good solar analogs ($0.55 \leq B-V \leq 0.75$). Three independent flux scales ($V-R$ [Duncan et al. 1991], $B-V$ [BC93], and $b-y$ [H96]) are in good agreement across this color range, with the $B-V$ scale of H96 having nearly the same slope as that of BC93 but systematically lower by about 12%. The three consistent flux scales agree closely with the T04 irradiance as well, as is also apparent in column (3) of Table 3.

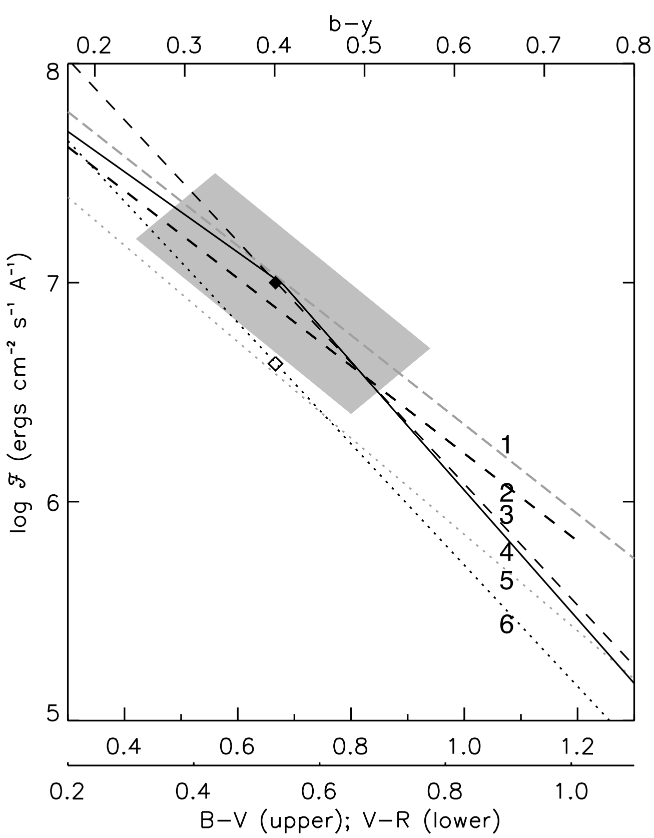

Fig. 2.—Comparison of several empirical flux scales: (1) BC93, $B-V$, deblanketed; (2) H96 $B-V$; (3) Duncan et al. (1991), deblanketed and based on L79 $V-R$; (4) H96 $b-y$; (5) BC93, unmodified (blanketed); and (6) L79. The gray area shows the main region of interest for the SSS program, and the open and filled diamonds show the surface and continuum HK fluxes in the bandpasses λ3925 to λ3975 for the Sun, derived from the T04 irradiance spectrum. Color scales on the *x*-axis are approximate.

Second, the BC93, H96 $B-V$, and H96 $b-y$ flux scales better replicate derived absolute surface fluxes for Vega (Hayes & Latham 1975; Tüg et al. 1977) than does the Duncan et al. (1991) $V-R$ relation. H96 found that they also better match the fluxes derived for warm stars, such as Procyon, that are part of the MWO and SSS target sets.

Finally, the inadequacy of $B-V$ as a temperature indicator in the red is apparent in the significant overestimation of surface flux for $B-V > 1.00$, whereas the original L79 flux scale and the H96 $b-y$ scale are in nearly perfect agreement.

These considerations lead to two conclusions. First, we have confidence in adopting the surface flux estimate derived from the T04 irradiance, as it stems from direct measurements rather than empirical relations, has the smallest uncertainty, and agrees well with the value predicted by three independently derived stellar flux scales. Second, because (1) we wish to establish a uniform solar-stellar calibration, and (2) Strömgren $b-y$ measurements are available for nearly all of our program stars (Olsen 1993, 1994a, 1994b), we employ the $b-y$ flux scale of H96 for determinations of surface flux in the continuum in this series of papers. This flux scale is as follows:

$$\log \mathcal{F}(\Delta\lambda) = 8.179 - 2.887(b-y), \ -0.10 \leq b-y \leq 0.41,$$

$$\log \mathcal{F}(\Delta\lambda) = 8.906 - 4.659(b-y), \ 0.41 < b-y \leq 0.80, \tag{3}$$

applicable to dwarfs only. The uncertainty on the surface fluxes obtained with this flux scale is 12% for stars with $b-y \leq 0.41$ and 16% for stars with $b-y > 0.41$.

This piecewise loglinear flux scale combines good agreement with the irradiance data, good replication of published surface fluxes over the $b-y$ range of nearly all the SSS targets (see § 4.3), and acceptable overall uncertainty of about 14%. For the few stars on our list without available $b-y$ measurements, we use the $B-V$ scale of BC93, since it appears to better replicate the irradiance measurement than does the analogous flux scale of H96.

4. MEASURING Ca ii H AND K EMISSION

4.1. *Bandpasses of Interest and MWO S*

Figure 3 shows the cores of the K and H lines (*left and right panels, respectively*) for several different spectra and with relevant bandpasses illustrated. This high-resolution K84 spectrum appears in black, along with two representative spectra from the much lower resolution SSS (the Sun [*dark gray*] and the active star HD 22049 = ε Eri [*light gray*]).

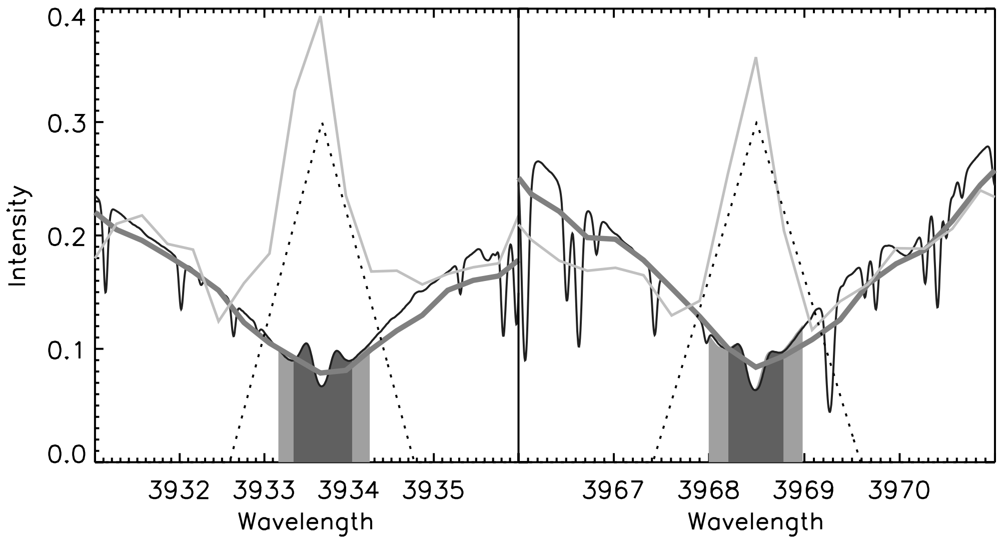

FIG. 3.—Measurement bandpasses at the cores of the Ca II K (*left*) and H (*right*) lines. The high-resolution K84 spectrum appears in black; SSS spectra of the Sun (*dark gray*) and HD 22049 (*light gray*) are overplotted. Other bandpasses discussed in the text include the MWO HKP-2 bandpasses (*dotted triangles*), the 1 Å HK index (*light-gray shaded region*), and the HK_1 index (*dark-gray shaded region*).

The HK index is the stellar or full-disk solar residual intensity in a rectangular 1 Å bandpass centered on the HK line cores (Fig. 3, *light-gray shaded region*). Wilson (1968, 1978) measured stellar fluxes in these bandpasses in the early years of the MWO stellar cycles program. White & Livingston (1978, 1981) also employed this quantity in their long-term solar monitoring program at the McMath telescope at Kitt Peak, as did the Sacramento Peak program (e.g., Keil & Worden 1984; Worden et al. 1998). At solar minimum, the NSO workers obtain mean HK indices of ~180 mÅ; the mean values from the 1996 and 2005 SSS spectra, near the extrema of cycle 23, are 188 and 186 mÅ, respectively.

A related quantity is the HK_1 index, or the total residual intensity between the H_1 and K_1 minima, which defines the boundary between purely photospheric emission (exterior to the minima) and emission that arises from both the chromosphere and photosphere (interior). This is illustrated by the dark-gray shaded region in Figure 3. For the Sun, the ratio is $HK/HK_1 \sim 1.7$ (this varies with activity; for the data of K84 illustrated in Fig. 1, it is 1.68).

Solar and stellar chromospheric activity is most commonly expressed, by dint of the sheer weight of the database, using the dimensionless S index obtained from the MWO spectrophotometers. Both the HKP-1 (1966–1977) and HKP-2 (post-1977) instruments at MWO collected data in four channels: two channels centered on the H and K line cores and two reference channels, commonly denoted R and V, located some distance redward and blueward, respectively, of the H and K lines. The H and K bandpasses of the HKP-2 are 1.09 Å FWHM triangles, shown by dotted lines in Figure 3.

The calibration of HKP-2 to HKP-1 data is discussed in detail by Vaughan et al. (1978), but for a general spectrum covering all the relevant bandpasses, $S = 8\alpha(H + K)/(R + V)$. Because the HKP-2 photometer used different R and V bandpasses than did the HKP-1, the correction factor α is used to calibrate the HKP-2 data to the HKP-1 data and is found to be 2.4 (Duncan et al. 1991). The factor of 8 accounts for the HKP-2 duty cycle (with an 8:1 ratio of core-to-continuum exposure time).

In principle, if one has a spectrum covering both H and K, as well as the HKP-2 reference bandpasses, one can measure S directly, either by replicating the triangular MWO bandpasses as closely as possible or by using different bandpasses as required by resolution and spectral coverage and adjusting α to obtain the best fit to the MWO ensemble. Wright et al. (2004) have recently done this with data obtained as part of the California and Carnegie Planet Search Project, although due to differences in calibration they needed to determine coefficients for each of the four quantities in S to match their values empirically to the MWO values. Similar determinations of S for nearby stars were made by Gray et al. (2003), using a value of 5 for α rather than 2.4. We can do the same with SSS spectra; using the 5 pixels (~1.5 Å) centered on the line cores for our H and K bandpasses (Fig. 3, *light-gray shaded areas*), we require $\alpha = 1.8$ to yield values of S consistent with MWO and other studies.

4.2. *Conversion between S and Surface Flux*

A well-established transformation between S and surface flux is desirable because the color term contained in S (due to its dependence on reference continua) requires conversion to a more physically interpretable quantity if maximum use is to be made of the MWO data, and because physical units are preferred for investigating connections between activity and essential stellar parameters such as rotation (e.g., Rutten & Schrijver 1987). Middelkoop (1982) and Rutten (1984) developed the relation that converts S to an arbitrary flux unit,

$$F_{\rm HK} = SC_{\rm cf}T_{\rm eff}^4 10^{-14}, \tag{4}$$

where $T_{\rm eff}$ is the effective temperature of the star, $C_{\rm cf}$ is a factor that removes the color term from S, and 10^{-14} is a scaling factor. Following Rutten (1984), we adopt

$$C_{\rm cf} = 0.25(B - V)^3 - 1.33(B - V)^2 + 0.43(B - V) + 0.24. \tag{5}$$

The arbitrary flux $F_{\rm HK}$ is then related to the absolute flux $\mathcal{F}_{\rm HK}$ by the simple relation

$$\mathcal{F}_{\rm HK} = KF_{\rm HK}. \tag{6}$$

For the Sun, taking $B - V_\odot = 0.642$ (Cayrel de Strobel 1996) and $T_{{\rm eff},\odot} = 5780$ K, we find $C_{\rm cf} = 1.082$ and, therefore,

$F_{HK} = 12.08S$. At solar minimum ($S \sim 0.164$; B95) we obtain $F_{HK} = 1.98$.

The T04 irradiance spectrum and the H96 $b - y$ flux scale yield the same value for the solar HK continuum flux ($\sim 10^7$ ergs cm^{-2} s^{-1} Å^{-1}). Converting the mean 1996 SSS solar HK index to the HK flux in a 1 Å rectangle yields $(1.88 \pm 0.22) \times 10^6$ ergs cm^{-2} s^{-1}, while a 1.09 Å triangle yields $(2.12 \pm 0.25) \times 10^6$ ergs cm^{-2} s^{-1}. The latter agrees with the $(2.17 \pm 0.32) \times 10^6$ ergs cm^{-2} s^{-1} derived by Oranje (1983) and Rutten (1984) using the Sacramento Peak Observatory (SPO) solar atlas (Beckers et al. 1976). (We take the errors in the Utrecht group's units to be 15%, i.e., dominated by the estimated uncertainty in the L79 $V - R$ flux scale on which they are based.) We therefore arrive at a back-of-the-envelope expected value of $(0.95 \pm 0.11) \times 10^6$ ergs cm^{-2} s^{-1} for the conversion factor K in equation (6) for flux measurements made with a 1 Å bandpass and $(1.07 \pm 0.13) \times 10^6$ ergs cm^{-2} s^{-1} for measurements using the HKP bandpasses. Uncertainties in the fluxes given above are those arising from the uncertainty in the $b - y$ flux scale, which is the dominant source of error in the surface flux estimate.

These estimates fall within a range of published values of K that differ by a factor of 2. These differences arise primarily from instrumental differences and varying estimates of the HK surface fluxes (blanketed or continuum) for cool main-sequence stars. We investigate the existing S-to-flux conversions in the next section.

4.3. *Evaluation of Complementary S Databases and S-to-Flux Conversions*

For all stars in our data set, including the Sun, we calculated a continuum flux using the H96 $b - y$ flux scale and an estimate of the effective temperature via the relation $\log T_{\rm eff} = 3.908 - 0.234(B - V)$ (Noyes et al. 1984). We measured the fluxes in 1 Å bandpasses centered on the H and K line cores and converted them to S via equations (4) and (6). The best regression between our S ensemble and that of B95 is achieved with $K = 0.97 \times 10^6$ ergs cm^{-2} s^{-1}, in excellent agreement with our estimate of 0.95×10^6 from the solar irradiance.

In Figure 4 we show the S values thus derived for every star overlapping our target set in the tables published by B95 (*bottom set of data*), Wright et al. (2004; *middle set of data*), and Gray et al. (2003; *top set of data*). For clarity, the Wright et al. and Gray et al. values are offset by 0.5 and 1.0 in S, respectively; the solid lines are of slope unity. Although there are significant outliers in each case, the general agreement among these four determinations of S is excellent; the rms scatter of each data set in S about the fit is 0.037 (B95), 0.025 (Wright et al. 2004), and 0.039 (Gray et al. 2003). However, we expect that some of the scatter in S is due to stellar variability rather than calibration error. For each data set in Figure 4, we have plotted stars for which we did not detect variability or that we classify as FA stars (see § 5.2) with large diamonds; the rms scatter of these stars alone about the regression is 0.011 (B95), 0.018 (Wright et al. 2004), and 0.012 (Gray et al. 2003).

We expect the best agreement between our S and the values of B95, since that is a comparison with the fundamental quantity rather than the derived S values in the other studies. This is in fact the case, and the excellent agreement between our values and those of B95 for low-variability stars (about 7% rms) suggests that (1) the $b - y$ flux scale does indeed provide good flux estimates for the entire color range of solar analogs ($\sim 0.340 \le b - y \le 0.550$), and (2) there is no systematic change in the quality of the SSS-MWO calibrations for inactive ($S \sim 0.150$) and fairly active ($S \sim 0.380$) Sun-like stars.

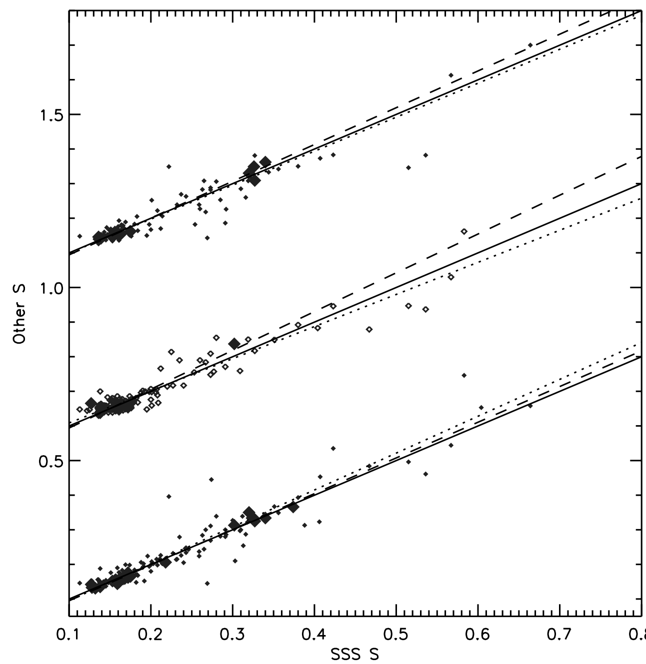

Fig. 4.—Comparison of the SSS ensemble with recent studies presenting calibrations of spectra to S. Grand mean S values are shown for B95 (*bottom set of data points and linear fits*), Wright et al. (2004; *middle set*), and Gray et al. (2003; *top set*). For clarity, the latter two data sets are offset by 0.5 and 1.0, respectively, in S. Solid lines of slope unity are drawn through each data set, while the dotted and dashed lines show the linear regressions on all stars and low-variability stars, respectively. Note in particular the excellent (7% rms) calibration of SSS S to that of B95 for low-variability stars.

Given the general agreement among all of these studies, which incorporate large numbers of stars, we consider the flux scale and transformation constant $K = 9.7 \times 10^5$ ergs cm^{-2} s^{-1} to yield acceptable measures of S and absolute stellar HK surface flux for the results presented in this study. The values thus derived also agree well with the values directly measured via the method described in § 4.2.

Several values of K have been presented in the literature, as summarized in Table 4. We can reconcile the discrepancies as follows.

We first note that the solar *absolute flux* measurements are in agreement. As noted above, Oranje (1983) and Rutten (1984) obtained $(2.17 \pm 0.32) \times 10^6$ ergs cm^{-2} s^{-1} for the HK surface flux in the HKP bandpasses near solar minimum using the SPO atlas; we calculate $(2.12 \pm 0.25) \times 10^6$ from the SSS data and the K84 atlas. However, our determination of the solar *arbitrary flux* at minimum is 1.98, in contrast to 1.797 given by Oranje (1983) and 1.69 given by Rutten (1984). Note that this unit depends only on $B - V$ and $T_{\rm eff}$, not the bandpass. The difference arises from the parameters used by those workers in equation (4); we assume $T_{{\rm eff},\odot} = 5780$ K and $(B - V)_\odot = 0.642$, whereas the other studies adopted 5660 K and 0.665 (Hardorp 1980; a determination that stands in contrast to the more recent examinations of Cayrel de Strobel 1996 and Gray 1995). Propagating the differences into equation (4) yields a 13% increase in the Oranje and Rutten arbitrary flux units, increasing them to 2.03 and 1.91, in reasonable agreement with our value.

With both the absolute and arbitrary surface fluxes reconciled, we are left to explain the discrepancies in K, which appear to arise from (1) the ~15%–20% uncertainties in the flux scales and (2) bandpass differences between the different programs. The original Middelkoop (1982) unit was based on the L79 fluxes, which are measured between the H_1 and K_1 minima. Because of

TABLE 4
Conversions of Arbitrary Flux F_{HK} to Physical Flux $\mathcal{F}_{HK}$

K (ergs cm $^{-2}$ s^{-1})	Based On	Reference
$(0.76 \pm 0.11) \times 10^6$	L79, HK_1 fluxes, $V - R$ flux scale	Middelkoop (1982)
$(0.80 \pm 0.15) \times 10^6$	1 Å rectangle, $V - R$ flux scale	Hall & Lockwood (1995)
$(0.97 \pm 0.11) \times 10^6$	1 Å rectangle, $b - y$ flux scale	This paper
$(1.21 \pm 0.16) \times 10^6$	HKP bandpasses, Beckers et al. (1976)	Oranje (1983)
$(1.29 \pm 0.19) \times 10^6$	HKP bandpasses, Beckers et al. (1976)	Rutten (1984)
$(1.52 \pm 0.22) \times 10^6$	HKP bandpasses	Schrijver et al. (1989a)

this, Oranje (1983) and Rutten (1984) developed a unit scaled upward to account for the ratio of the flux measured in HKP bandpasses to that in the HK_1 bandpasses. For the quiet Sun, we measure a ratio of $\mathcal{F}_{HKP}/\mathcal{F}_{HK_1} = 1.82$, while for the 1 Å bandpass we find $\mathcal{F}_{HK}/\mathcal{F}_{HK_1} = 1.68$. However, the Middelkoop (1982) unit was derived from measured surface fluxes of the very active L79 stars, and the flux ratio for these targets is smaller; $\mathcal{F}_{HK_1}$ is a larger fraction of flux in the 1 Å and HKP bandpasses both because the line core is more pronounced and because the separation of the H_1 and K_1 minima increases with increasing luminosity (Ayres 1979). For the active stars in the L79 sample, $\mathcal{F}_{HK}/\mathcal{F}_{HK_1} \sim 1.2$; applying this correction to Middelkoop's unit yields $K = 0.91 \times 10^6$, agreeing well with the 0.97×10^6 we derive from our stellar ensemble. If we scale the Oranje-Rutten units to represent (1) the surface flux in a 1 Å bandpass and (2) the $\mathcal{F}_{HK}/\mathcal{F}_{HK_1}$ ratio for the active stars on which Middelkoop's relation was based, they become 0.93 and 0.99×10^6. The one value of K we cannot fully reconcile is that of Schrijver et al. (1989a), which was derived using an arbitrary flux $F_{HK} = 10.8S$. We find that F_{HK} is ~12% larger than this; using this value in the conversion would change Schrijver et al.'s unit to 1.35 ± 0.20, which explains about half the discrepancy but does not agree, within the estimated uncertainties, with the value we adopt for this work.

The arguments above also require a reexamination of our own conversion unit (Hall & Lockwood 1995) of 0.80×10^6. The present paper employs a flux scale that gives higher surface flux estimates (and a lower estimated error of 12% vs. 19%) for solar analogs than the scale we employed previously and better matches the new T04 solar irradiance data. Thus, our previous unit also must increase to recover the same values of S. The *relative* solar-stellar S-flux calibrations are not affected, since we apply the same flux scale to all targets, but the *absolute* calibration is revised upward.

We conclude with the following back-of-the-envelope summary of our final S-to-flux conversion:

1. The HK 1 Å or HKP surface flux for an inactive solar analog is, very roughly, 2×10^6 ergs cm^{-2} s^{-1}.
2. The arbitrary surface flux at solar minimum, obtained using widely accepted values of the solar color and temperature, is roughly 2.00.
3. As shown by equation (6), $\mathcal{F}_{HK} = KF_{HK}$.
4. Therefore, K cannot be very different from 1×10^6, and the appropriate value to use is bandpass-dependent, being $\sim(0.95 \pm 0.11) \times 10^6$ for absolute surface fluxes measured in a 1 Å rectangle and determined using our $b - y$ flux scale and about 10% higher for those measured using the HKP bandpass. Such values will provide consistent transformations to S for both the Sun and Sun-like stars.

4.4. *Measurement of Magnetic Emission in the H and K Lines*

A perennial complication in the interpretation of S or surface flux measurements of the Ca II H and K lines is the presence of flux arising from nonmagnetic sources. Hartmann et al. (1984) and Noyes et al. (1984) defined the chromospheric emission fraction $\log R'$, assuming that the flux internal to the H_1 and K_1 minima above zero flux is chromospheric, and that the flux passed by the HK photometer external to the minima is photospheric. The quantity $R_{HK} = C_{cf}S$ corrects S for the varying photospheric component in an ensemble of stars; Noyes et al. (1984) then derived

$$\log R_{phot} = -4.898 + 1.918(B - V)^2 - 2.893(B - V)^3, \quad (7)$$

from which follows $R'_{HK} = R_{HK} - R_{phot}$. It is trivial to generate $\log R'$ from our data and useful to do so as a consistency check. But since we are particularly interested in the variability (or lack thereof) of the magnetic component of the emission, it is desirable to use the surface fluxes themselves as the fundamental data.

Let us reconsider Figure 4 and define "wing" to mean those portions of the H and K lines in our 1 Å bandpass exterior to the H_1 and K_1 minima and "core" to mean those portions interior to these points. Following the analysis of Schrijver et al. (1989b), we consider our measured 1 Å flux $\mathcal{F}_{1\,Å}$ to contain components arising from the RE atmosphere, an underlying "basal" flux (whether of magnetic or mechanical origin), and the magnetic flux of primary interest here. (Schrijver et al.'s analysis was for the MWO photometer bandpasses, but the same arguments apply to our 1 Å rectangle.)

Kelch et al. (1979) and L79 present measurements of fluxes in the H and K line cores for a number of dwarf stars also on our program, as well as essential line parameters (including core widths and RE corrections). We first calculated expected line core widths $\Delta\lambda_{HK_1}$ for "inactive" stars (those for which no emission reversal is apparent in our spectra, which includes stars of $S \leq 0.175$), using the published widths and fluxes, along with the scaling relation $\Delta\lambda_{HK_1} \propto (\mathcal{F}_{NR,*}/\mathcal{F}_{NR,\odot})^{1/4}$ (Ayres 1979), to determine the run of inactive star line widths as a function of $b - y$, where $\mathcal{F}_{NR}$ is the emission from the nonradiatively heated chromosphere in the line cores. Using the K84 solar spectrum degraded to our resolution, we used grafted synthetic emission profiles of varying strength onto various line core widths to determine the fraction of the emission in a 1 Å bandpass lying exterior to the K1 and H1 minima. Then, for any SSS measurement, we use the measured K2 peaks and the expected core widths to determine the fraction of the surface flux lying exterior to the HK_1 minima, and we take this to be the photospheric contribution $\mathcal{F}_{phot}$. The relations that emerge are displayed in Figure 5. As noted above, for the Sun $\mathcal{F}_{phot}$ is about 40%, while for more active stars it decreases to 10% or less. This interpretation is somewhat complicated by the well-known variation of the line wing intensity with activity (e.g., White & Livingston 1981). We therefore expect the $\mathcal{F}_{K1}/\mathcal{F}_{1\,Å}$ ratios shown in Figure 5 (*bottom*) to be systematically slightly

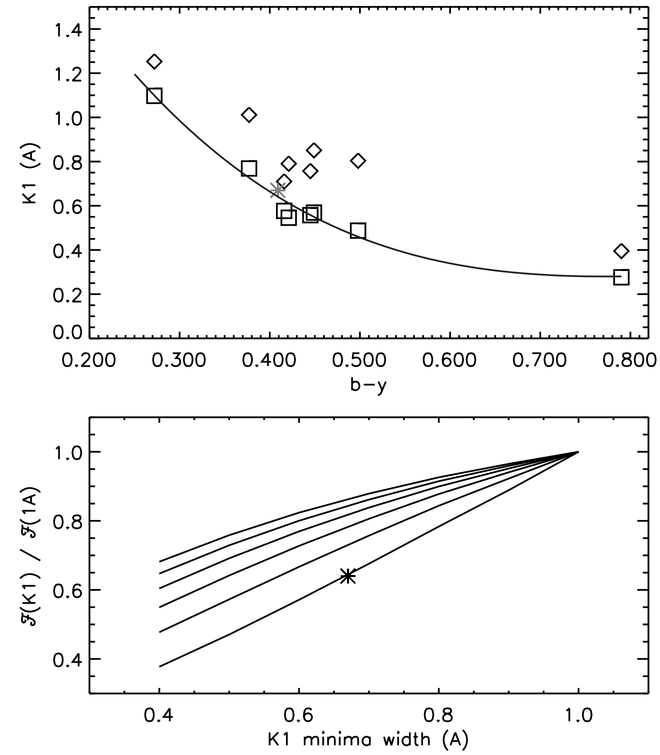

FIG. 5.—Estimation of the fraction of flux in our 1 Å bandpass lying in the H and K line cores (i.e., within the H_1 and K_1 minima). *Top*: Separation in angstroms of the K_1 minima in several dwarf stars as measured by Kelch et al. (1979, *diamonds*) and scaled to "inactive" (i.e., solar minimum) level using the $\mathcal{F}^{1/4}$ scaling law of Ayres (1979, *squares*). The solid line shows the best fit to the inactive star K_1 widths. *Bottom*: Fraction of the flux in the 1 Å bandpass lying within the K_1 minima for stars with K2 peaks ranging from solar levels (*bottom line*; the mean Sun is shown by an asterisk) up to 6 times the solar level ($I_{K2} \sim 0.5$). Similar relations hold for the H line, and the estimates are combined to remove the photospheric flux from each SSS 1 Å flux measurement.

overestimated, since the K84 solar spectrum will underestimate $\mathcal{F}_{\rm phot}$ for K3 emission significantly higher than that observed at solar maximum. However, a 40% increase in the K3 intensity in the full-disk Sun corresponds to only a 2% increase in the K1 wing intensity (e.g., Fig. 8 in White & Livingston 1981). The effect of this systematic error on the present results is that (1) the magnetic emission for the most active stars will be overestimated by a few percent and (2) the variability will be slightly damped by a similar amount, due to the small amount of residual photosphere in the final surface fluxes. This is well below the overall uncertainty arising from the flux scales and does not alter the conclusions in § 5.

In Figure 6 we show the mean photosphere-subtracted fluxes $\mathcal{F}' = \mathcal{F}_{1\,\text{Å}} - \mathcal{F}_{\rm phot}$ for all 143 stars in our target set. The well-known color-dependent "basal" emission $\mathcal{F}_{\rm min}$ is apparent as an obvious color-dependent minimum flux. This concept of a basal flux was developed in the 1980s (e.g., Rutten 1986; Schrijver 1987; Schrijver et al. 1989b). Subtraction of this flux from the total line core flux yields the so-called excess flux, typically denoted in the literature by $\Delta\mathcal{F}_{\rm Ca}$ and interpreted as the component of the surface flux arising from magnetic sources. (The basal flux itself may arise from acoustic heating or magnetic sources unrelated to the dynamo; see, e.g., the review by Schrijver 1995.) The papers from the Utrecht group examined $\mathcal{F}_{\rm min}$ as it is manifested in the MWO bandpasses; the values derived here are lower, since they represent the basal flux between the H1 and K1

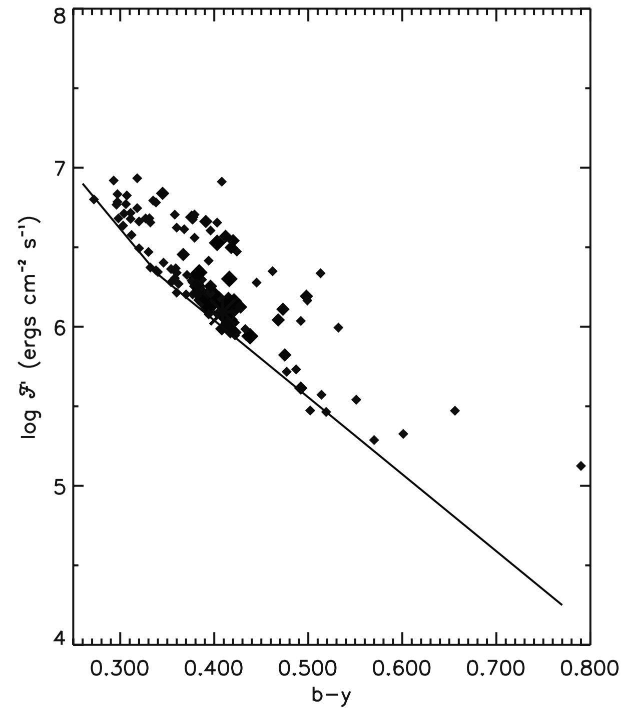

FIG. 6.—Mean $H_1 + K_1$ fluxes for all 143 of our targets. These fluxes were derived by removing the photospheric contribution exterior to the H_1 and K_1 minima as described in the text. Large symbols indicate high-priority targets. A well-defined minimum $H_1 + K_1$ flux is apparent, defined by the loglinear relation given in the text, and determined by a fit to the lowest flux stars in several $b - y$ bins.

minima only. From a fit to the lowest activity stars in a set of color bins spanning $0.250 \le b - y \le 0.800$, we obtain

$$\log \mathcal{F}_{\rm min} = \begin{array}{ll} 8.752 - 7.125(b-y), & b-y \le 0.340, \\ 7.975 - 4.837(b-y), & b-y > 0.340. \end{array}$$

Applying all the corrections yields the desired component of our 1 Å measurements: $\Delta\mathcal{F}_{\rm Ca} \equiv \mathcal{F}_{1\,\text{Å}} - \mathcal{F}_{\rm phot} - \mathcal{F}_{\rm min}$. This serves as the fundamental datum for all results reported below.

5. SOLAR AND STELLAR CHROMOSPHERIC VARIABILITY

5.1. *Representative Time Series*

We present time series of the excess flux in 54 of the highest priority stars in the survey in Figures 7 and 8. All panels are scaled in units of 10^5 ergs cm^{-2} s^{-1}, and the maximum and minimum seasonal mean solar excess fluxes in these units are indicated by dashed and dotted lines, respectively. Each panel is annotated with the HD number of the target, its $b - y$ color, our mean computed S, and the total number of observations. Figure 7 shows the time series for our priority 1 stars (except HD 95128, which was added to this list only recently), as well as the Sun. The priority 2 stars, HD 95128, and a few priority 3 stars are shown in Figures 8*a* and 8*b*. The panels in each figure are arranged in order of increasing $b - y$.

Each panel in Figures 7 and 8 shows individual observations (*dots*), as well as seasonal means (*diamonds*). Error bars are shown for the seasonal means; they are derived from the errors on the individual observations, which are in turn derived following Howell (2000), using the measured ADUs in the line cores of each extracted spectrum and the known gain (40 e^- ADU^{-1}) and read

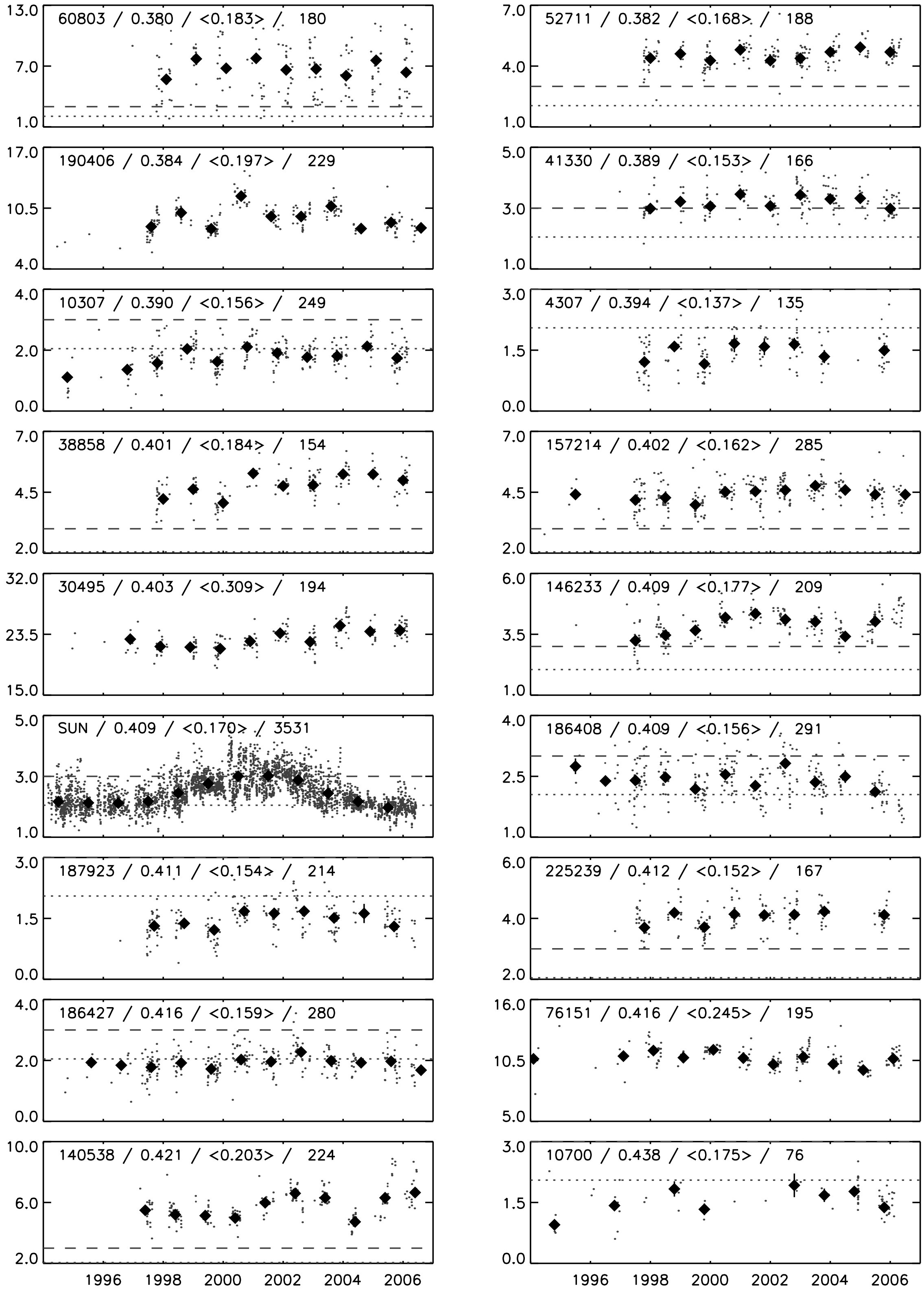

FIG. 7.—Time series for priority 1 stars (except for the recently added HD 95128) and the Sun. The *y*-axes show $\Delta\mathcal{F}_{\rm Ca}$ in units of 10^5 ergs cm^{-2} s^{-1}. The dotted and dashed lines show solar minimum and maximum, respectively, and they are displayed on every panel where they appear within the scaling. Annotations in each panel show the HD number, $b-y$, mean *S*, and number of observations. Stars are arranged in order of increasing $b-y$. The Sun is by far our best-sampled target, and each solar observation is the average of 16 1 s exposures, so the activity record is cleaner than that of any of the stellar targets.

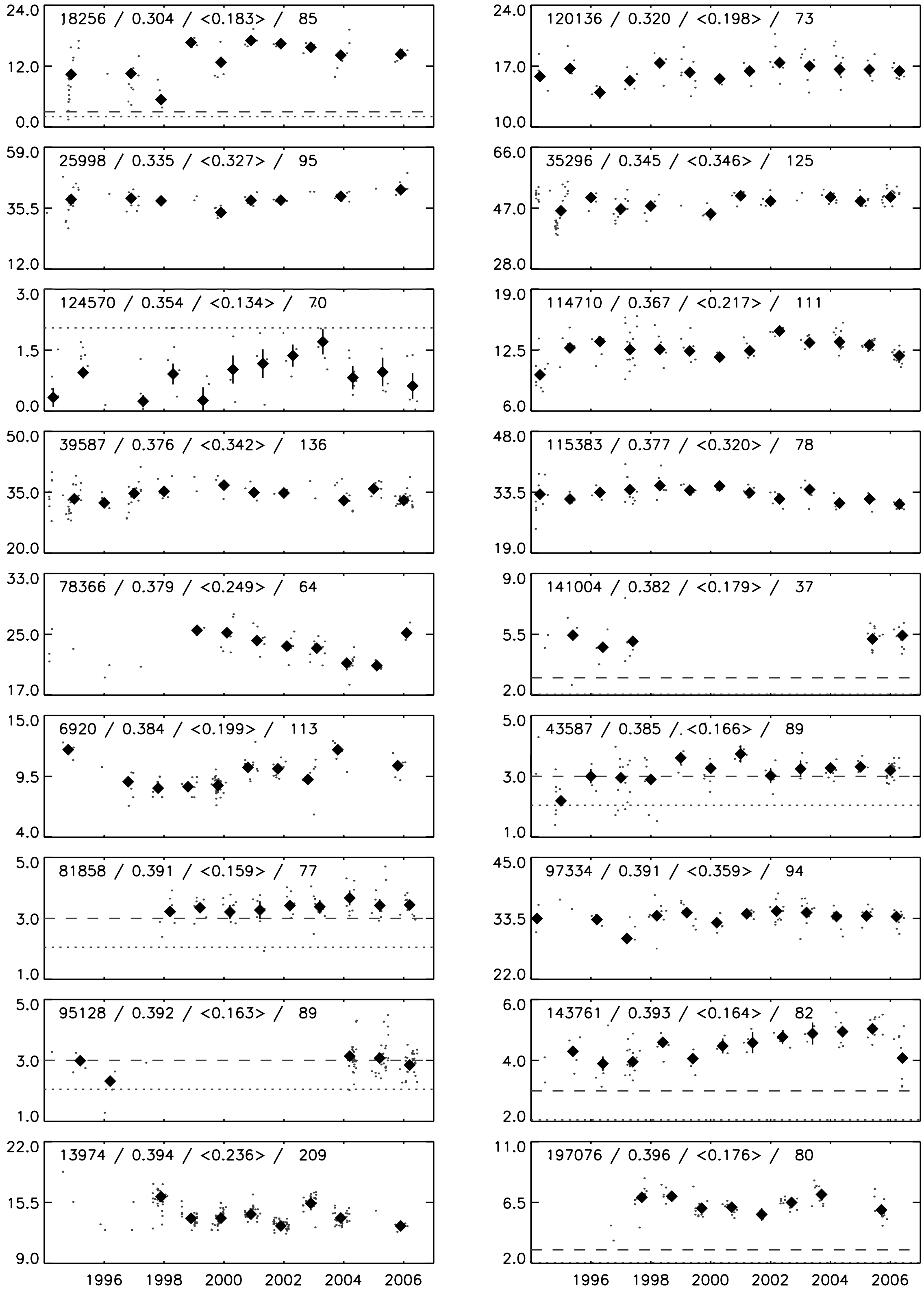

FIG. 8*a*

FIG. 8.— Time series for priority 2 stars, HD 95128, and priority 3 stars with the densest sampling. Scaling and annotation are the same as in Fig. 7. The 36 representative time series are arranged in order of increasing $b - y$.

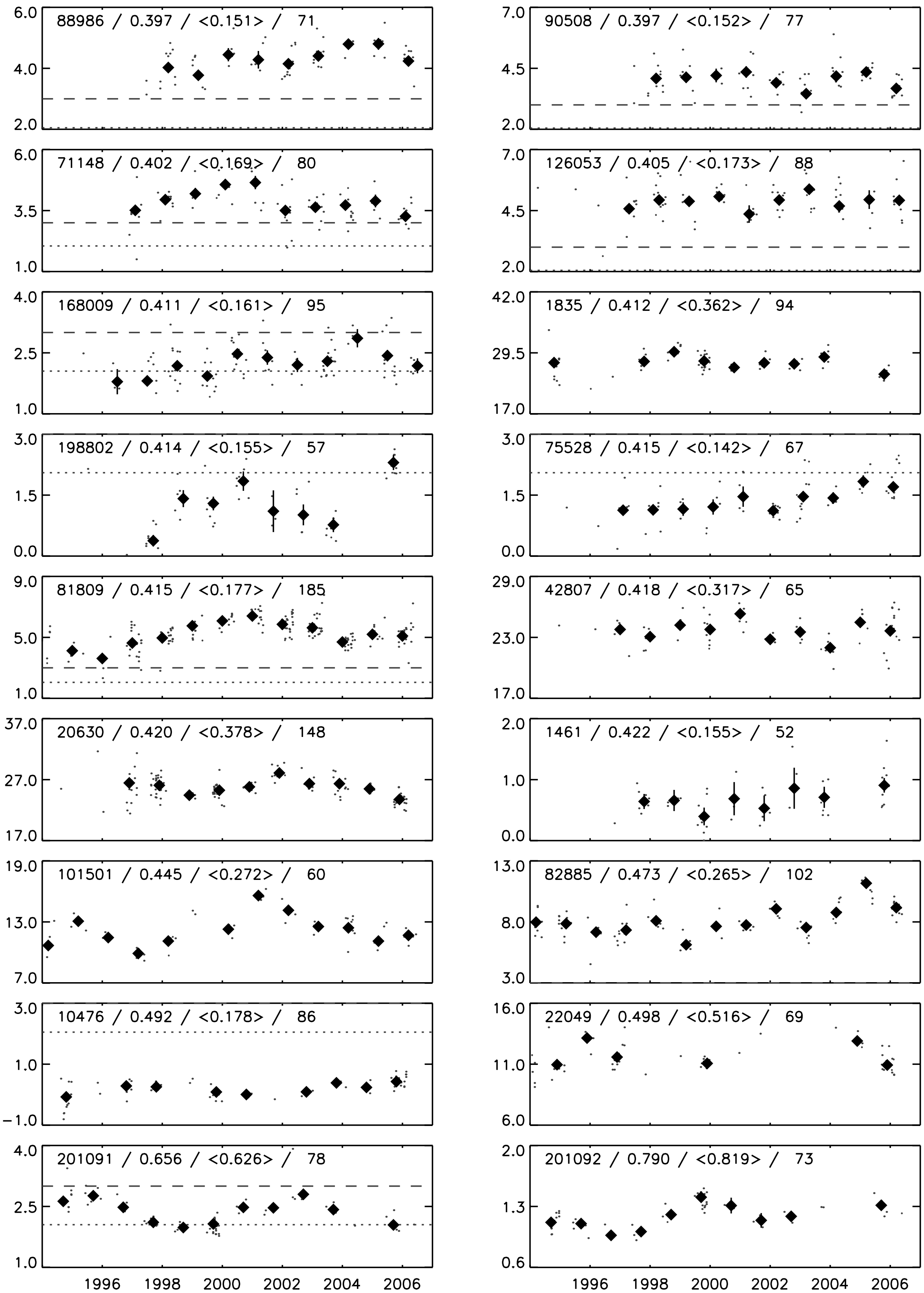
88986 / 0.397 / <0.151> / 71
90508 / 0.397 / <0.152> / 77
71148 / 0.402 / <0.169> / 80
126053 / 0.405 / <0.173> / 88
168009 / 0.411 / <0.161> / 95
1835 / 0.412 / <0.362> / 94
198802 / 0.414 / <0.155> / 57
75528 / 0.415 / <0.142> / 67
81809 / 0.415 / <0.177> / 185
42807 / 0.418 / <0.317> / 65
20630 / 0.420 / <0.378> / 148
1461 / 0.422 / <0.155> / 52
101501 / 0.445 / <0.272> / 60
82885 / 0.473 / <0.265> / 102
10476 / 0.492 / <0.178> / 86
22049 / 0.498 / <0.516> / 69
201091 / 0.656 / <0.626> / 78
201092 / 0.790 / <0.819> / 73
1996
1998
2000
2002
2004
2006

FIG. 8*b*

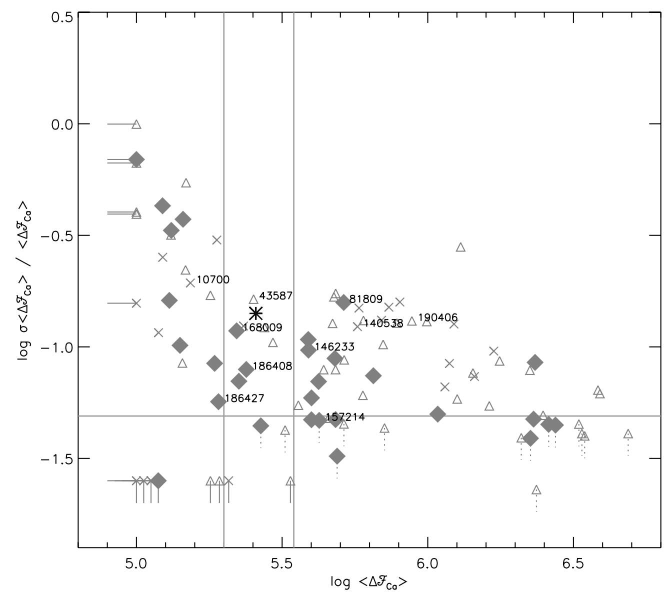

FIG. 9.—Mean excess flux vs. rms variability about the mean. Vertical lines show the solar excess flux at minimum and maximum. Diamonds indicate solar analogs with $0.395 \leq b - y \leq 0.430$, while triangles indicate warmer stars ($b - y < 0.395$) and crosses indicate cooler stars ($b - y < 0.430$). The Sun is indicated by the asterisk. Stars aligned at minimum flux and rms values indicate nondetections of excess flux and significant variability. Stars discussed in § 5.4 are labeled with their HD number. Symbols with solid lines extending downward and to the left represent nondetections (variability class N in Table 5). Symbols with dashed lines extending downward represent FA stars in Table 5.

noise (42 e^- pixel^{-1}), and taking sky and dark current to be negligible (both assumptions are justifiable, given our bright sources and relatively short exposures). We define the mean for the *i*th season as the usual weighted average of the *n* observations for that season, i.e., $\langle \Delta\mathcal{F}_{\rm Ca}\rangle_i = \Sigma(\Delta\mathcal{F}_n/\sigma_n^2)/\Sigma(1/\sigma_n^2)$. The uncertainty of the seasonal means is shown by the vertical error bars; where an error bar is not visible for a given mean, it is smaller than the size of the plot symbol.

5.2. *Mean Activity and Long-Term Variability*

A general picture of the variability of targets is presented in Figure 9. We include all stars for which we have five or more seasonal means with 3–20 observations per observing season, under the assumption that this should reveal at least half the variability amplitude for cycling stars with typical 6–10 yr cycle periods. As of 2006 May, we had 99 targets that meet these criteria, including the Sun and all priority 1 and 2 stars. In Figure 9 we show the grand mean $\langle \Delta\mathcal{F}_{\rm Ca}\rangle$ for each target versus the rms of the seasonal mean excess flux about the mean, $(\sigma\langle \Delta\mathcal{F}_{\rm Ca}\rangle)/\langle \Delta\mathcal{F}_{\rm Ca}\rangle$; for simplicity of nomenclature, we refer to this quantity hereafter with the expression $\sigma_\mathcal{F}/\mathcal{F}$. In Figure 9 the Sun is shown by the asterisk, with the vertical lines showing the solar excursion in excess flux and the horizontal line showing variability that is one-third of that of solar cycles 22–23. Symbols indicate ranges of color; stars closest to the solar color ($0.395 \leq b - y \leq 0.430$) are indicated by diamonds.

The observational variance in the time series for each target was determined from simulated, normally distributed Monte Carlo time series with zero mean and uncertainties equal to the measured values. Not surprisingly, the uncertainties are large for low-activity targets in which $\Delta\mathcal{F}_{\rm Ca}$ is close to our detection limit, and for these stars this quantity may be close to, or even below (due to intrinsic errors), zero. From the known 1 Å HK surface fluxes and the total ADUs collected in the H and K line cores for solar analog spectra of typical S/N, we find that $\Delta\mathcal{F}_{\rm Ca} \sim 0$ within the errors if the deduced $\Delta\mathcal{F}_{\rm Ca}$ is less than $\sim 8 \times 10^4$ ergs cm^{-2} s^{-1}. In such cases, we effectively detect no excess flux, and negative individual or seasonal mean $\Delta\mathcal{F}_{\rm Ca}$ appear in the time series. In Figure 9, stars for which the observed variability is less than that expected from the observational uncertainty are marked with a solid line extending downward. Stars with $\Delta\mathcal{F}_{\rm Ca}$ at or below the detection limit are plotted with an ordinate of $\log \Delta\mathcal{F}_{\rm Ca} = 5.0$ and a solid line extending to the left.

The quantitative data for Figure 9 are assembled in Table 5, including the mean excess flux (in units of the solar mean), as well as the mean log R'. We also assign each target a general variability class corresponding to one of the following cases:

Nondetections (*N*).—There are 13 targets for which the observed variability is zero within the errors or for which $\Delta\mathcal{F}_{\rm Ca}$ is below our detection limit. They are marked on Figure 9 with solid lines extending downward or to the left, respectively.

Flat activity (*FA*) *stars*.—There are 14 targets for which $\sigma_\mathcal{F}/\mathcal{F}$ is nonzero but less than or equal to one-third of that of the Sun. This criterion has been applied in other studies to identify FA stars (e.g., B95) in terms of *S*, so we adopt it here to facilitate comparison between this work and other studies. This definition allows inclusion of stars with known variability but high mean levels of activity (e.g., HD 20630 and HD 35296), but it is easy to discriminate between them. These stars are marked on Figure 9 with dashed lines extending downward from the symbol.

Variable stars.—The vertical lines denoting the solar excursion in $\Delta\mathcal{F}_{\rm Ca}$ divide Figure 9 into three activity regimes; we designate stars that are not in one of the two classifications above as low-activity variables (LV), solar-activity variables (SV), and high-activity variables (HV). We consider a star to lie in the SV regime if (1) it has $\langle \Delta\mathcal{F}_{\rm Ca}\rangle$ within the solar cycle 23 excursion of excess flux and (2) it has $\sigma_\mathcal{F}/\mathcal{F} > 0.33(\sigma_\mathcal{F}/\mathcal{F})_\odot$ (this is the region of Fig. 9 lying above the horizontal line and between the vertical lines). There are 17, 9, and 46 targets in these categories, respectively.

In Figure 10 we show the mean $\Delta\mathcal{F}_{\rm Ca}$ for our 143 targets and the Sun, plotted against the familiar quantities log R' and *S*. The pairs of dotted lines show the solar excursion in $\Delta\mathcal{F}_{\rm Ca}$, log R', and *S*, and the Sun is plotted with an asterisk. Filled diamonds indicate solar analogs with $0.395 \leq b - y \leq 0.430$, while open diamonds and squares indicate targets bluer and redder than this range, respectively. The symbol size is proportional to the variability of the seasonal means; larger symbols indicate more variable stars. Finally, the horizontal dashed lines indicate rough regimes at which Maunder minimum stars have frequently been considered to lie, e.g., $S \sim 0.145$ (White et al. 1992) and log $R' \sim -5.1$ (Henry et al. 1996; Gray et al. 2003; Wright 2004), while the vertical dashed line indicates $\Delta\mathcal{F}_{\rm Ca}$ of one-third of the value at solar minimum.

For the Sun, only ∼13% of the surface flux contained in the 1 Å flux measurements appears to be of magnetic origin, which explains the relative insensitivity of *S* to log $\Delta\mathcal{F}_{\rm Ca}$ in Figure 10—stars lying within the solar excursion in *S* exhibit excess fluxes of order $5.0 \leq \log \Delta\mathcal{F}_{\rm Ca} \leq 5.8$, or from roughly 40% to 200% of the solar minimum and maximum yearly means, respectively. Likewise, we also observe a number of stars in the subsolar *S* regime (∼0.145–0.155) that show near-solar excess flux; however, very few low-*S* stars have $\Delta\mathcal{F}_{\rm Ca}$ above the present solar maximum. Thus, low-*S* stars may be, but are not necessarily, in magnetically inactive states. The converse is also true: we observe low-$\Delta\mathcal{F}_{\rm Ca}$ stars with *S* comparable to the solar values (HD 10700 = τ Cet being a prime example; see individual star commentaries in § 5.4).

This broad distribution of excess flux levels in these low-variability stars is apparent in Figures 11 and 12, in which we

TABLE 5
Excess Flux and Variability of Well-Observed Stars

HD	Seasons	No. of Obs.	$\langle \log R' \rangle$	$\langle \delta \mathcal{F}_{Ca} \rangle (\odot = 1.00)$	$\sigma_{\mathcal{F}}/\mathcal{F}$	Class
Sun	12	3531	−4.94	1.00	0.144	SV
123	8	81	−4.59	5.66	0.073	HV
1461	8	51	−5.04	0.25	. . .	N
1835	9	82	−4.41	10.7	0.049	HV
4307	8	134	−5.16	0.56	0.085	LV
6920	10	110	−4.81	3.89	0.132	HV
10307	11	245	−5.02	0.71	0.177	LV
10476	9	70	−4.98	0.17	0.897	LV
10700	8	67	−4.94	0.58	0.193	LV
13421	10	56	−5.24	0.00	. . .	N
13974	8	200	−4.69	5.60	0.077	HV
15335	6	20	−5.19	0.58	0.214	LV
16739	6	19	−4.94	1.41	0.063	HV
18256	10	63	−4.87	5.06	0.274	HV
18757	5	15	−5.11	1.05	0.121	SV
19373	8	29	−5.02	0.70	. . .	N
19994	5	18	−4.95	1.84	0.127	HV
20630	10	144	−4.40	10.2	0.044	FA
22049	6	58	−4.44	4.41	0.085	HV
25680	6	45	−4.53	9.16	0.086	HV
25998	8	67	−4.44	15.3	0.064	HV
30495	10	188	−4.49	9.05	0.048	HV
30562	8	56	−5.15	0.56	0.373	LV
32923	6	44	−5.15	0.27	. . .	N
35296	10	95	−4.40	19.0	0.041	FA
38858	9	154	−4.87	1.87	0.088	HV
39587	10	99	−4.43	13.5	0.040	FA
41330	9	165	−5.02	1.27	0.041	FA
42807	10	61	−4.50	8.83	0.039	FA
43587	12	85	−4.95	1.22	0.166	SV
48682	5	17	−4.93	2.35	0.060	HV
50692	5	18	−4.96	2.02	0.090	HV
52711	9	188	−4.86	1.79	0.048	HV
60803	9	179	−4.86	2.81	0.102	HV
70110	8	48	−5.11	0.52	0.318	LV
71148	10	80	−4.94	1.52	0.108	HV
75332	6	25	−4.60	15.0	0.064	HV
75528	10	65	−5.12	0.50	0.163	LV
76151	10	189	−4.66	4.24	0.052	HV
78366	8	55	−4.64	8.79	0.079	HV
78418	5	18	−4.93	2.28	0.149	HV
79028	6	24	−5.18	0.76	. . .	N
81809	12	178	−4.95	1.79	0.161	HV
81858	9	76	−5.07	1.02	. . .	N
81997	7	33	−4.67	9.21	0.021	FA
82885	12	87	−4.68	3.15	0.159	HV
88737	8	24	−4.61	9.76	0.051	HV
88986	9	68	−5.07	1.39	0.069	HV
90508	9	73	−5.03	1.56	0.061	HV
95128	5	81	−5.02	1.13	0.104	SV
97334	11	87	−4.42	13.21	0.042	FA
100180	8	27	−4.95	2.35	0.131	HV
101177	5	15	−4.97	1.60	0.034	FA
101501	11	52	−4.62	4.82	0.126	HV
102870	5	26	−4.99	1.88	0.147	HV
103095	8	29	−5.21	0.46	0.252	LV
107213	5	15	−5.13	0.31	. . .	N
107705	5	24	−4.73	3.07	0.130	HV
109358	7	34	−4.99	1.88	0.078	HV
114710	12	100	−4.76	4.56	0.059	HV
115383	12	66	−4.47	12.9	0.045	FA
115404	5	18	−4.57	2.85	0.150	HV
115617	7	29	−4.93	0.80	. . .	N
117176	9	53	−5.28	0.00	. . .	N
120136	12	68	−4.79	6.37	0.054	HV
121370	6	20	−5.25	0.00	. . .	N
124553	8	54	−4.90	1.84	0.173	HV
124570	12	63	−5.27	0.31	. . .	N
124850	5	23	−4.69	8.24	0.038	FA
126053	10	81	−4.91	1.93	0.030	FA
131511	5	19	−4.52	4.48	0.066	HV
140538	10	217	−4.80	2.25	0.126	HV
141004	5	31	−4.94	2.02	0.042	FA
142373	5	32	−5.18	1.08	0.122	SV
143761	12	74	−5.03	1.72	0.080	HV
146233	10	203	−4.93	1.52	0.097	HV
149661	10	43	−4.68	2.73	0.134	HV
152391	7	24	−4.48	6.60	0.095	HV
157214	11	277	−5.00	1.66	0.046	FA
158614	7	31	−5.01	0.19	. . .	N
159222	5	19	−4.92	1.80	0.073	HV
163840	8	75	−5.02	0.87	0.070	SV
168009	11	91	−5.00	0.84	0.116	SV
176051	5	20	−4.92	2.79	0.043	FA
176095	6	23	−4.78	6.92	0.083	HV
181655	5	36	−4.99	0.73	0.095	LV
185144	11	58	−4.87	0.74	0.305	LV
186408	12	286	−5.05	0.68	0.078	SV
186427	12	273	−5.04	0.75	0.059	LV
187923	10	210	−5.04	0.53	0.103	LV
190406	10	221	−4.80	3.43	0.129	HV
197076	8	77	−4.94	2.55	0.074	HV
198802	8	55	−5.04	0.48	0.429	LV
199960	7	46	−5.07	0.51	0.342	LV
201091	10	60	−4.76	0.91	0.124	SV
201092	9	51	−4.98	0.46	0.114	LV
216385	7	32	−5.10	0.55	0.543	LV
217014	6	44	−5.03	0.08	. . .	N
225239	8	166	−5.04	1.56	0.047	HV

present histograms of the distributions of the seasonal mean activity levels in $\log R'$ and $\Delta\mathcal{F}_{Ca}$, respectively, for our targets. In each figure we show our priority 1 and 2 targets in light gray (48 stars) and the priority 3 targets (143 stars) in medium gray. Over a decade of observing, we have obtained occasional observations of a total of 311 Sun-like stars, and the distribution of this full sample is shown in dark gray. The solar observations are shown by a black histogram, scaled to fit on the plot. The bimodal distribution of activity in $\log R'$ noted by Gray et al. (2003, 2006) is evident in Figure 11, although it is less pronounced due to the skew of our target set toward low-activity solar analogs.

In both figures, histogram elements marked with crosses indicate the grand mean $\log R'$ and $\Delta\mathcal{F}_{Ca}$ for the 27 stars in Table 5 that currently qualify as nondetections or FA stars. In both cases, the targets classified as nondetections or FA stars separate into well-defined groups. Eight of them are found to be active ($\log R' \geq -4.75$) but with only moderate cyclic or irregular variability relative to their mean (e.g., HD 20630, 35296, and 39587). Ten exhibit near-solar levels of excess magnetic flux but relatively little variability (HD 41330 and 157214 being two especially well-observed examples). Finally, nine lie clearly below the present solar minimum. We therefore identify 19 stars, or about 20% of the sample in Table 5, with solar or subsolar activity levels and little or no long-term variability. They are about equally divided between stars with Sun-like $\Delta\mathcal{F}_{Ca}$ and very inactive stars with <5.0 (i.e.,

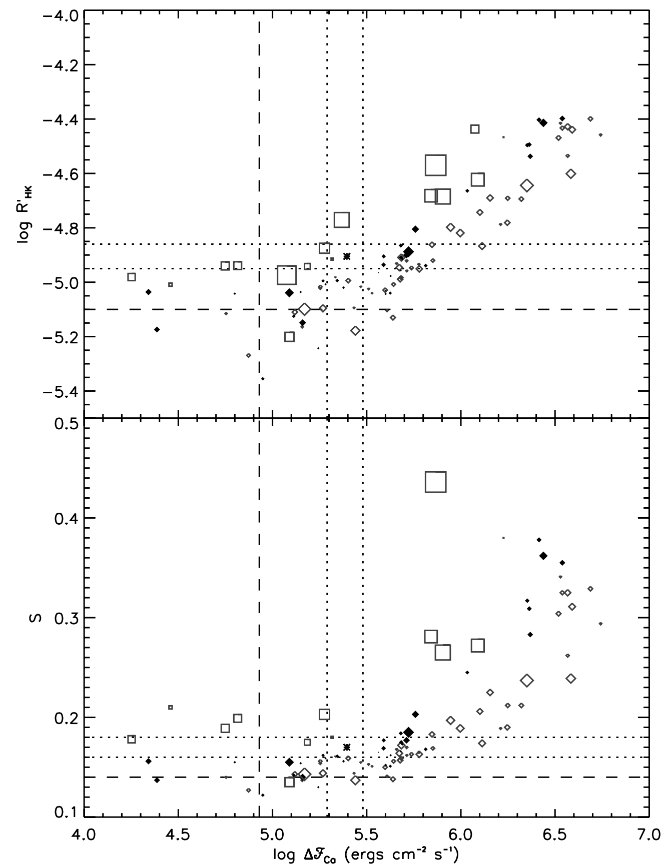

FIG. 10.—Excess flux $\log \Delta\mathcal{F}_{\rm Ca}$ for 143 stars and the Sun, plotted against the chromospheric emission fraction $\log R'$ (*top*) and MWO S (*bottom*). Dotted lines show the extent of the solar cycle; horizontal dashed lines show typical $\log R'$ and S values for putative Maunder minimum stars. The vertical dashed line is at $\Delta\mathcal{F}_{\rm Ca} = 0.33\Delta\mathcal{F}_{\rm Ca\odot}$. Symbols give a rough indication of temperature. Warm stars ($b - y \leq 0.395$) are shown by open diamonds, cool stars ($b - y \geq 0.430$) by open squares. Solar analogs lying between these limits are shown by filled diamonds.

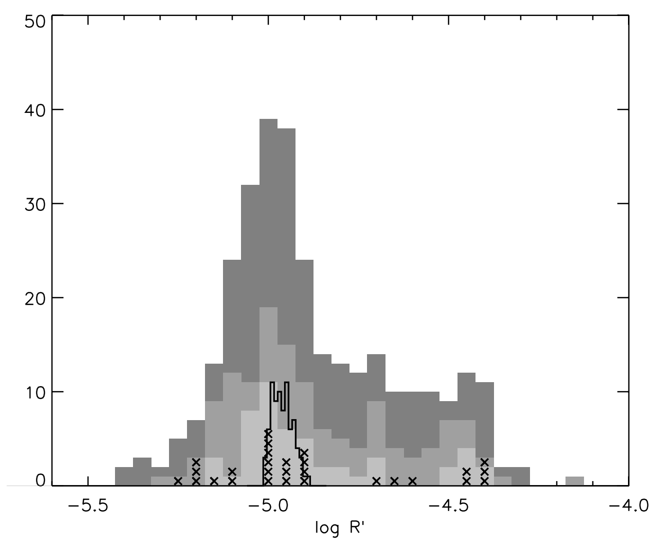

FIG. 11.—Overall distribution of mean $\log R'$ for our targets. The three shades of gray indicate the distribution of the solar analogs ($0.395 \leq b - y \leq 0.430$, *light gray*), the 143 stars in our present target set (*medium gray*), and all 311 stars we have ever observed (*dark gray*). The black histogram shows the solar observations, greatly scaled down to fit on the plot. Histogram elements marked with crosses indicate FA stars, defined as those for which the standard deviation of the seasonal mean HK_1 fluxes is less than one-third of the solar value.

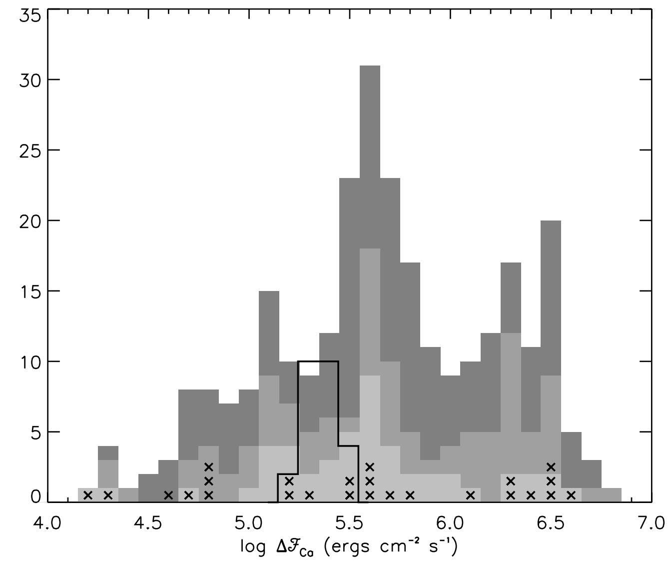

FIG. 12.—Same as Fig. 11, but for the distribution of excess flux rather than $\log R'$. In this plot the crosses indicate stars for which $\sigma\langle\Delta\mathcal{F}_{\rm Ca}\rangle \leq 0.33\,\sigma\langle\Delta\mathcal{F}_{\rm Ca\odot}\rangle$.

near or below our detection limit). As with the $\log R'$ and S distributions, we find no evidence that weakly varying stars necessarily lie in subdued magnetic states relative to the modern solar minimum.

5.3. *Chromospheric and Coronal Flux in Solar Analogs*

Several authors have examined the relationship between the MWO HK time series and stellar UV and X-ray emission, generally finding that chromospheric excess flux is related to coronal emission by simple power laws. Schrijver et al. (1992) obtained $\mathcal{F}_{\rm X} \propto \Delta\mathcal{F}_{\rm Ca}^{1.50\pm0.20}$, independent of color. Hempelmann et al. (1996) obtained exponents of 0.99 ± 0.13 for MWO stars they classified as "constant" or "regular" MWO stars (meaning FA or well-defined cycles) and 1.7 ± 0.14 for "irregular" stars, suggesting that different dynamo modes operate in these two samples.

A total of 39 stars from Table 5 overlap the sample set employed by Hempelmann et al. (1996). Our $\Delta\mathcal{F}_{\rm Ca}$ plotted against the *ROSAT* All Sky Survey (RASS) fluxes used by those authors appear in Figure 13. Vertical lines show the solar excursion in $\Delta\mathcal{F}_{\rm Ca}$ as usual, and the data points indicate stars with chromospheric variability greater than the Sun's (*black filled diamonds*), less than the Sun's (*gray filled diamonds*), and zero within the errors (*open diamonds*). Discarding stars at or below our detection limit ($\log \Delta\mathcal{F}_{\rm Ca} \leq 4.9$), a linear fit to our entire sample yields a result essentially identical to that of the full sample of Hempelmann et al. (1996): $\mathcal{F}_{\rm X} \propto \Delta\mathcal{F}_{\rm Ca}^{1.41\pm0.09}$, with a σ value of 0.27. However, this interpretation is made problematic by both the presence of different types of variability in the members of the target set and the highly uncertain data points below $\log \Delta\mathcal{F}_{\rm Ca} \sim 5.0$, where the measurable excess chromospheric flux is close to zero and the X-ray fluxes are upper limits.

Our target set overlaps the Hempelmann et al. (1996) unambiguously irregular stars for only three targets, marked with crosses in Figure 13. This arises from our sample bias toward the closest solar analogs, which eliminates many of the cool, irregularly varying stars in the MWO sample. We therefore cannot evaluate the steeper power law for the irregular stars. We do find that for all stars of $\langle\log \Delta\mathcal{F}_{\rm Ca}\rangle > 5.3$, $\mathcal{F}_{\rm X} \propto \Delta\mathcal{F}_{\rm Ca}^{1.64\pm0.11}$. A near-unity slope is obtained if we include all the points in Figure 11, but we

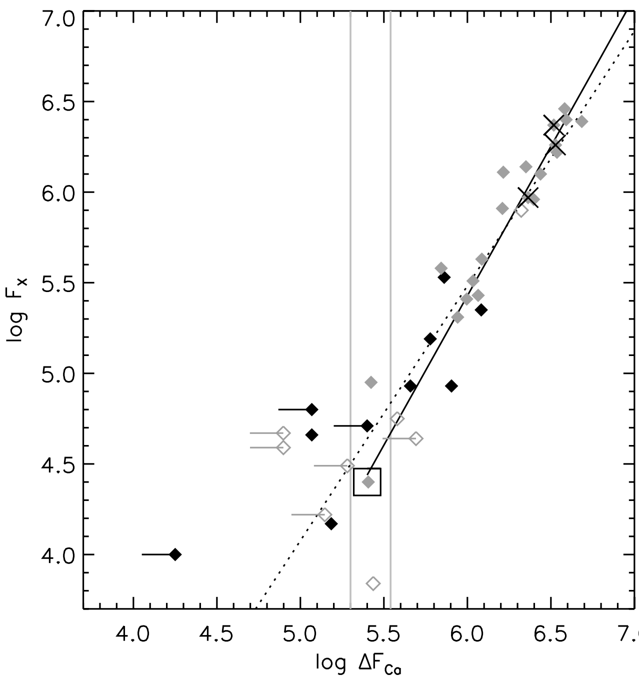

FIG. 13.—Coronal flux (from *ROSAT* measurements) vs. excess chromospheric flux. The good solar analogs are well matched by a power law with exponent 1.41. The square shows the location of the mean Sun.

regard our data for $\Delta\mathcal{F}_{Ca}$ as unreliably near zero and have not included them here.

5.4. *Commentary on Individual Stars*

Below are summary comments on several stars of particular interest (detailed discussions of these and other targets of special interest will appear in the third paper of this series). We group them into broad categories: stars that are or have been considered good solar analogs, stars that may be examples of stellar Maunder minimum states, and other targets. Within each category, we discuss the targets in order of increasing HD number.

5.4.1. *Cycling Stars*

HD 81809 (Fig. 8*b*).—The well-determined cycle of 8.17 ± 0.08 yr (B95) is recovered in our continued observations of this star, with a minimum in the 2004 season. Combination of our data with the MWO time series yields 8.22 yr (J. C. Hall et al. 2007, in preparation). However, HD 81809 is a binary with evolved components (e.g., Pourbaix 2000), so the system is not considered a solar analog.

HD 146233 (*18 Sco,* Fig. 7).—This is the currently accepted best "solar twin," on the basis of the similarity of its physical parameters to those of the Sun (Porto de Mello & da Silva 1997; Soubiran & Triaud 2004), as well as its temporal photometric (Lockwood et al. 2002) and spectroscopic (Hall & Lockwood 2000) behavior. The HK emission reached a minimum in 2004, followed by a rapid rise in the most recent two observing seasons, which has yielded a better estimate of the cycle period. Combining our data series with MWO data from 1992 to 2001, kindly supplied by S. L. Baliunas, and using a Scargle periodogram (Horne & Baliunas 1986), we obtain a period of 7.1 yr. The mean excess flux is somewhat higher than the Sun's, corresponding to *S* values ∼0.010–0.015 higher than the solar values, but the cycle amplitude is nearly identical.

HD 190406 (*15 Sge,* Fig. 7).—The short period allows us to obtain a cycle period of 2.4 ± 0.3 yr (B95 obtain 2.60 ± 0.02, with a 16.9 yr secondary period). Within the limitations of the seasonal resolution, there is evidence for highly variable cycle amplitudes, with a pronounced maximum in 1999 and no significant rise for the "expected" maximum of 2005.

5.4.2. *Maunder Minimum Candidates*

HD 10700 (τ *Cet, G8 V,* Fig. 7).—This star exhibits a mostly FA record in the lengthy MWO series, with evidence of a rise beginning in 1989 (B95). Our derived $\langle S\rangle = 0.175$ well matches the mean MWO value and lies near the midpoint of solar cycles 22–23. Judge et al. (2004) have found that while the chromospheric spectrum of τ Cet is similar to that of the Sun near minimum, its transition region and coronal emission place it very close to the basal limit of Rutten et al. (1991). Judge et al. (2004) propose that τ Cet is in a grand minimum analogous to the solar Maunder minimum. We find $\langle\Delta\mathcal{F}_{Ca}\rangle = 0.58\langle\Delta\mathcal{F}_{Ca\odot}\rangle$ with no evidence of cyclic or long-term variability. It is, in fact, classified in Table 5 as LV, i.e., a low-activity variable. We consider this a weak result, however, since (1) we have fewer observations and (2) much of the variance arises from two poorly sampled seasons. Further monitoring of this very bright target will be done.

HD 43587 (Fig. 8*a*).—B95 classify this star as "Flat?" We find evidence of variability comparable to the solar cycle 23 excursion prior to 2002, followed by zero variability from 2002 to 2006. No cyclic behavior is evident in the time series, and $\langle\Delta\mathcal{F}_{Ca}\rangle$ is near the upper bound of the present solar excursion.

HD 140538 (ψ *Ser, G5 V,* Fig. 7).—This is the most intriguing example of a possible Maunder minimum transition in our data set (see Fig. 9). For the four seasons from 1997 through 2000, this star exhibited a FA record, but then it appears to have switched to a vigorously cycling mode with a period of about 4 yr, beginning in 2000. The pre-2000 variability is zero within the errors, while the present cycle has an amplitude approximately twice that of solar cycle 23. If this is in fact a transition from a noncycling to a cycling state, it is interesting to note that (1) the activity level of this star is above that of solar maximum ($\langle S\rangle = 0.204$, $\langle\Delta\mathcal{F}_{Ca}\rangle \cong 2.5\langle\Delta\mathcal{F}_{Ca\odot}\rangle$), and (2) the seasonal mean $\Delta\mathcal{F}_{Ca}$ at the 2004 cycle minimum is slightly below that observed during the putative noncycling seasons.

5.4.3. *Other Stars*

HD 10476 (*107 Psc,* Fig. 8*b*).—Although this star exhibits one of the best-defined cycles of the MWO stars (9.6 ± 0.1 yr; B95), its X-ray luminosity is quite low relative to stars of its type, at only 0.34 dex above HD 10700 in the RASS observations (Schmitt & Liefke 2004). While the cycle is apparent in our data, the derived $\Delta\mathcal{F}_{Ca}$ is considerably less than that for HD 10700.

HD 157214 (*72 Her,* Fig. 7).—Our $\langle S\rangle$ of 0.163 is very near the modern solar minimum, but the star is warmer than the Sun ($b - y = 0.402$) and shows evidence of an ∼9 yr cycle with an amplitude of ∼30% of that of solar cycle 23. Two to three more observing seasons will be required to confirm the existence or absence of an activity minimum in 2007–2008.

HD 168009 (Fig. 8*b*).—This star is declared one of the Top Ten solar analogs (Soubiran & Triaud 2004) and, along with 18 Sco, is one of the closest points to the Sun in the $\Delta\mathcal{F}_{Ca}$-variability plane (Fig. 9). We find $\langle S\rangle = 0.161$ and $\langle\Delta\mathcal{F}_{Ca}\rangle = 2.15\times10^5$ ergs cm^{-2} s^{-1}, both comparable to the low-activity Sun. However, no periodicity appears in the present data series, and the irregular variability is comparable to that of the present solar cycle.

HD 186408 and 186427 (*16 Cyg A and B,* Fig. 7).—While these stars are both technically classified LV, the variability is only slightly above the observational uncertainties. No significant peaks are apparent in the periodograms, and both stars lie consistently below the Sun in $\Delta\mathcal{F}_{\rm Ca}$ and S.

6. CONCLUSIONS

We have summarized the broad properties of the mean excess chromospheric flux and its variability in an ensemble of 143 Sun-like stars and the Sun itself. We draw the following conclusions about the general magnetic activity and variability of this magnitude-limited ($V \leq 7.5$) sample of solar analogs:

1. For the set of 99 targets in Table 5 (98 stars plus the Sun), 72 exhibit variability of excess magnetic flux $\Delta\mathcal{F}_{\rm Ca}$ of at least one-third of that of the Sun over cycles 22 and 23. Of the remaining stars, 14 can be confidently classified as flat activity (FA) stars, with detectable variability of less than one-third of that of the Sun, while the remaining 13 have variability or excess flux that is zero within the errors.
2. The FA stars are found across the solar cycle excursion in both log R' and $\Delta\mathcal{F}_{\rm Ca}$.
3. Among stars exhibiting excess magnetic flux $\Delta\mathcal{F}_{\rm Ca}$ within the excursion of solar cycles 22–23, HD 43587 and HD 168009 are found to be the good solar analogs (i.e., stars with gross characteristics similar to those of the Sun) closest to the Sun in their overall magnetic activity level and variability (Fig. 11), although their cycle characteristics differ significantly from the Sun's. Other stars in this regime are either not solar analogs (e.g., HD 201092) or have much sparser data sets (e.g., HD 95128 and HD 142373) and will require further observation.
4. The currently most widely acknowledged "solar twin," 18 Sco (HD 146233), has an activity cycle comparable in amplitude to the Sun's but somewhat shorter, with a period of $\sim$7 yr. Its mean $\Delta\mathcal{F}_{\rm Ca}$ is estimated to be $\sim$50% higher than that of the mean Sun, corresponding to a mean S of 0.185.
5. Identification of Maunder minimum candidates is an important aspect of our survey. Since a noncycling state does not imply a low absolute magnetic activity level (in either log R' or $\Delta\mathcal{F}_{\rm Ca}$), we consider it most useful to look for transitions between cycling and noncycling states. In the present target set, the star HD 140538 presents the most significant example of a clear transition between a noncycling state and a pronounced cycling state, beginning in the 2000 observing season and entering a cycling state with an $\sim$4 yr period.

The authors thank the referee, Jeffrey Linsky, for a careful and well-considered review that clarified a number of points in this paper. Further papers in this series will examine the echelle data and the detailed records of stars of particular interest, incorporating observations taken subsequent to those reported in this paper. The SSS project is supported by grant ATM-0447159 from the National Science Foundation. This research has made use of the SIMBAD database, operated at CDS, Strasbourg, France.

REFERENCES

Arvesen, J. C., Griffin, R. N., & Pearson, D. P. 1969, Appl. Optics, 8, 2215
Ayres, T. R. 1979, ApJ, 228, 509
Baliunas, S. L., Donahue, R. A., Soon, W., & Henry, G. W. 1998, in ASP Conf. Ser. 154, Tenth Cambridge Workshop on Cool Stars, Stellar Systems, and the Sun, ed. R. A. Donahue & J. A. Bookbinder (San Francisco: ASP), 153
Baliunas, S. L., & Jastrow, R. 1990, Nature, 348, 520
Baliunas, S. L., & Vaughan, A. H. 1985, ARA&A, 23, 379
Baliunas, S. L., et al. 1995, ApJ, 438, 269 (B95)
Barnes, T. G., & Evans, D. S. 1976, MNRAS, 174, 489
Barnes, T. G., Evans, D. S., & Parsons, S. B. 1976, MNRAS, 174, 503
Beasley, A. J., & Cram, L. E. 1993, ApJ, 417, 157 (BC93)
Beckers, J. M., Bridges, C. A., & Gilliam, L. B. 1976, A High Resolution Spectral Atlas of the Solar Irradiance from 380 to 700 Nanometers (Hanscom AFB: Sacramento Peak Obs., Air Force Geophys. Lab)
Blanco, C., Catalano, S., & Marilli, E. 1976, A&A, 48, 19
Blanco, C., Catalano, S., Marilli, E., & Rodono, M. 1974, A&A, 33, 257
Breger, M. 1976, ApJS, 32, 1
Cayrel de Strobel, G. 1996, A&A Rev., 7, 243
Duncan, D. K., et al. 1991, ApJS, 76, 383
Eberhard, G., & Schwarzschild, K. 1913, ApJ, 38, 292
Eddy, J. A. 1976, Science, 192, 1189
Fligge, M., & Solanki, S. 2000, Geophys. Res. Lett., 27, 2157
Fontenla, J., White, O. R., Fox, P. A., Avrett, E. H., & Kurucz, R. L. 1999, ApJ, 518, 480
Foukal, P., & Lean, J. L. 1990, Science, 247, 556
Fröhlich, C. 2000, in Solar Variability and Climate, ed. E. Friis-Christensen et al. (Dordrecht: Kluwer), 28
Gray, D. F. 1995, PASP, 107, 120
Gray, R. O., Corbally, C. J., Garrison, R. F., McFadden, M. T., Bubar, E. J., McGahee, C. E., O'Donoghue, A. A., & Knox, E. R. 2006, AJ, 132, 161
Gray, R. O., Corbally, C. J., Garrison, R. F., McFadden, M. T., & Robinson, P. E. 2003, AJ, 126, 2048
Haisch, B., & Schmitt, J. H. M. M. 1996, PASP, 108, 113
Hall, J. C. 1996, PASP, 108, 313 (H96)
Hall, J. C., & Lockwood, G. W. 1995, ApJ, 438, 404
———. 2000, ApJ, 545, L43
Hardorp, J. 1978, A&A, 63, 383
———. 1980, A&A, 88, 334
Hartmann, L., Soderblom, D., Noyes, R., Burnham, N., & Vaughan, A. H. 1984, ApJ, 276, 254
Hayes, D. S., & Latham, D. W. 1975, ApJ, 197, 593
Hempelmann, A., Schmitt, J. H. M. M., & Stepien, K. 1996, A&A, 305, 284
Henry, G. W. 1999, PASP, 111, 845
Henry, T. J., Soderblom, D. R., Donahue, R. A., & Baliunas, S. L. 1996, AJ, 111, 439
Horne, J. H., & Baliunas, S. L. 1986, ApJ, 302, 757
Howell, S. B. 2000, Handbook of CCD Astronomy (Cambridge: Cambridge Univ. Press)
Judge, P. G., Saar, S. H., Carlsson, M., & Ayres, T. R. 2004, ApJ, 609, 392
Keil, S. L., & Worden, S. P. 1984, ApJ, 276, 766
Kelch, W. L., Linsky, J. L., & Worden, S. P. 1979, ApJ, 229, 700
Kurucz, R. L., Furenlid, I., Brault, J., & Testerman, L. 1984, Solar Flux Atlas from 296 to 1300 nm (Sunspot, NM: Natl. Sol. Obs.) (K84)
Lang, K. R. 1992, Astrophysical Data I: Planets and Stars (New York: Springer)
Lean, J. L., Beer, J., & Bradley, R. 1995, Geophys. Res. Lett., 22, 3195
Lean, J. L., & Foukal, P. 1988, Science, 240, 906
Linsky, J. L., & Ayres, T. R. 1978, ApJ, 220, 619
Linsky, J. L., Worden, S. P., McClintock, W., & Robertson, R. M. 1979, ApJS, 41, 47 (L79)
Lockwood, G. W., Hall, J. C., Skiff, B. A., Radick, R. R., Baliunas, S. L., Soon, W., & Donahue, R. A. 2002, BAAS, 34, 651
Lockwood, G. W., Skiff, B. A., Baliunas, S. L., & Radick, R. R. 1992a, Nature, 360, 653
Lockwood, G. W., Skiff, B. A., & Radick, R. R. 1997, ApJ, 485, 789
Lockwood, G. W., Tüg, H., & White, N. M. 1992b, ApJ, 390, 668
Middelkoop, F. 1982, A&A, 107, 31
Neckel, H., & Labs, D. 1984, Sol. Phys., 90, 205
Noyes, R. H., Hartmann, L., Baliunas, S. L., Duncan, D. K., & Vaughan, A. H. 1984, ApJ, 279, 763
Olsen, E. H. 1993, A&AS, 102, 89
———. 1994a, A&AS, 104, 429
———. 1994b, A&AS, 106, 257
Oranje, B. J. 1983, A&A, 124, 43
Pasquini, L., Pallavicini, R., & Pakull, M. 1988, A&A, 191, 253
Porto de Mello, G. F., & da Silva, L. 1997, ApJ, 482, L89
Pourbaix, D. 2000, A&AS, 145, 215
Radick, R. R. 1992, in ASP Conf. Ser. 27, The Solar Cycle, ed. K. L. Harvey (San Francisco: ASP), 450
Radick, R. R., Lockwood, G. W., Skiff, B. A., & Baliunas, S. L. 1998, ApJS, 118, 239
Ribes, J. C., & Nesme-Ribes, E. 1993, A&A, 276, 549
Rutten, R. G. M. 1984, A&A, 130, 353
———. 1986, A&A, 159, 291
Rutten, R. G. M., & Schrijver, C. J. 1987, A&A, 177, 155
Rutten, R. G. M., Schrijver, C. J., Lemmens, A. F. P., & Zwaan, C. 1991, A&A, 252, 203

Schmitt, J. H. M. M., & Liefke, C. 2004, A&A, 417, 651
Schrijver, C. J. 1987, A&A, 172, 111
———. 1995, A&A Rev., 6, 181
Schrijver, C. J., Coté, J., Zwaan, C., & Saar, S. H. 1989a, ApJ, 337, 964
Schrijver, C. J., Dobson, A. K., & Radick, R. R. 1989b, ApJ, 341, 1035
———. 1992, A&A, 258, 432
Soubiran, C., & Triaud, A. 2004, A&A, 418, 1089
Strassmeier, K. G. 2005, Astron. Nachr., 326, 269
Taylor, B. J. 1998, in IAU Symp. 189, Fundamental Stellar Properties: The Interaction between Observation and Theory, ed. T. R. Bedding, A. J. Booth, & J. Davis (Dordrecht: Kluwer), 83
Thekaekara, M. P., Kruger, R., & Duncan, C. H. 1969, Appl. Optics, 8, 1713
Thuillier, G., et al. 1998, Sol. Phys., 177, 41
———. 2004, in Solar Variability and Its Effects on Climate, ed. J. M. Pap & P. Fox (Geophys. Monogr. 141; Washington: AGU), 171 (T04)
Tüg, H., & Schmidt-Kaler, M. 1982, A&A, 105, 400
Tüg, H., White, N. M., & Lockwood, G. W. 1977, A&A, 61, 679
Vaughan, A. H., Preston, G. W., & Wilson, O. C. 1978, PASP, 90, 267
Wagner, R. M. 1992, in ASP Conf. Ser. 23, Astronomical CCD Observing and Reduction Techniques, ed. S. B. Howell (San Francisco: ASP), 160
Wang, Y.-M., Lean, J. L., & Sheeley, N. R. 2005, ApJ, 625, 522
White, O. R., & Livingston, W. C. 1978, ApJ, 226, 679
———. 1981, ApJ, 249, 798
White, O. R., Livingston, W. C., Keil, S. L., & Henry, T. W. 1998, in ASP Conf. Ser. 140, Synoptic Solar Physics, ed. K. S. Balasubramaniam, J. Harvey, & D. Rabin (San Francisco: ASP), 293
White, O. R., Skumanich, A., Lean, J. L., Livingston, W. C., & Keil, S. L. 1992, PASP, 104, 1139
Willstrop, R. V. 1965, MmRAS, 69, 83
Wilson, O. C. 1968, ApJ, 153, 221
———. 1978, ApJ, 226, 379
Worden, J. R., White, O. R., & Woods, T. N. 1998, ApJ, 496, 998
Wright, J. T. 2004, AJ, 128, 1273
Wright, J. T., Marcy, G. W., Butler, R. P., & Vogt, S. S. 2004, ApJS, 152, 261
Zhang, Q., Soon, W. H., Baliunas, S. L., Lockwood, G. W., Radick, R. R., & Skiff, B. A. 1994, ApJ, 427, L111